Development of innovative flow fields in a vanadium redox flow battery: design of channel obstructions with the aid of 3D computational fluid dynamic model and experimental validation through locally-resolved polarization curves

M. Messaggi[a], C. Gambaro[b], A. Casalegno[a], M. Zago[a,*]

[a] Politecnico di Milano, Department of Energy, Via Lambruschini 4, 20156 Milano, Italy

[b] Eni DR&D Renewable Energy and Environmental R&D Center, Via Fauser 4, 28100, Novara, Italy

* corresponding author: matteo.zago@polimi.it

Abstract

Distribution of the electrolyte over the porous electrode is a critical issue limiting the power density of vanadium redox flow batteries. The flow field design involves a trade-off among high battery performance, low pressure drops, reduced electrolyte imbalance and thus the understanding of the physical phenomena regulating mass transport of the electrolyte is crucial to develop improved flow fields. This work firstly presents the development of a 3D computational fluid dynamic model that couples fluid dynamic analysis of the electrolyte with the electrochemistry of the reactions involved. The model simulates the influence of both single serpentine and interdigitated flow field. After extensive validation with respect to local polarization curves in symmetric cell with both positive and negative electrolyte, the model is used to design flow fields with two different channel obstructions: the first one is located at the channel wall, while the second one is placed close to electrode interface. Both obstructions create a localized pressure difference between adjacent channels, enhancing electrolyte permeation through porous electrode. Finally, model predictions are verified experimentally: considering cycling operation at different operating current densities, the second obstruction

is more effective in obtaining a good trade-off among performance, pressure drops and evolution of exchanged capacity.

Keywords: *CFD, channel obstructions, flow-field, interdigitated, model, VRFB.*

Nomenclature

List of symbols

$\mathcal{A}$	Fitting parameter of mass transport coefficient h_m [-]
a	Specific active area [$m^2\ m^{-3}$]
c	Molar concentration [$mol\ m^{-3}$]
D	Diffusivity of vanadium ions [$m^2\ s^{-1}$]
E_{eq}	Equilibrium potential [V]
F	Faraday constant [$C\ mol^{-1}$]
$\boldsymbol{f}$	Volume force vector [$N\ m^{-3}$]
h_m	Mass transport coefficient [$m\ s^{-1}$]
i	Current density [$A\ m^{-2}$]
i_R	Reaction rate [$A\ m^{-3}$]
k_0	Reaction rate constant [$m\ s^{-1}$]
M	Molarity [$mol\ l^{-1}$]
MM	Molar mass [$kg\ kmol^{-1}$]
N	Species molar flux [$mol\ m^{-2}\ s^{-1}$]
p	Pressure [Pa]
Q	Flow rate [$m^3\ s^{-1}$]
R	Universal gas constant [$J\ mol^{-1}\ K^{-1}$]
T	Temperature [K]
$\boldsymbol{u}$	Velocity vector [$m\ s^{-1}$]
u_i	Species mobility [$mol\ s\ kg^{-1}$]
V	Voltage [V]
x	Mass fraction [-]
z	Charge number [-]

Greek symbols

α	Charge transfer coefficient [-]
β_F	Forchheimer drag coefficient [m^{-1}]
ε	Porosity of compressed electrode [-]
η^*	Overpotential [V]
κ	Permeability [m^2]
μ	Viscosity [Pa s]
ρ	Density [$kg\ m^{-3}$]
ϕ	Potential [V]

Superscripts

II-III	Relative to V^{2+} - V^{3+} reaction
IV-V	Relative to VO^{2+} - VO_2^+ reaction
b	Relative to bulk
eff	Effective properties
s	Relative to surface
T	Transposed

Subscripts

-	Relative to negative electrode
acid	Relative to sulphuric acid
H^+	Relative to protons
HSO_4^-	Relative to hydrogen sulphate ions
i	Relative to i-th chemical species
l	Relative to electrolyte
m	Relative to mass
out	Relative to channel outlet
R	Relative to electrochemical reactions
s	Relative to solid phase
SO_4^{2-}	Relative to sulphate ions
V	Relative to Vanadium
V^{2+}	Relative to V^{2+} ion - Vanadium (II)
V^{3+}	Relative to V^{3+} ion - Vanadium (III)
VO^{2+}	Relative to VO^{2+} ion - Vanadium (IV)
VO_2^+	Relative to VO_2^+ ion - Vanadium (V)

Glossary

CFD	Computational fluid dynamics
OCV	Open circuit voltage
PRESTO!	Pressure staggering options
SIMPLE	Semi implicit method for pressure linked equations
SoC	State of charge
VRFB	Vanadium redox flow battery

1. Introduction

The vanadium redox flow battery (VRFB) is a promising technology for energy storage because of its peculiarity to decouple power and stored energy, its high efficiency and long charge-discharge cycle life [1–4]. Moreover, VRFB employs four oxidation states of a single chemical species, leading to reversible cross-contamination between the two half cells. However, VRFBs commercialization is still hindered by technological issues, among which the distribution of the electrolyte over the porous electrode is one of the most important [4–6], as it considerably affects system power density [7,8]. The flow pattern imposed by the flow field is crucial in the definition of pressure drops, electrolyte velocities and ions concentration distribution. Thus, flow field geometry regulates auxiliary consumption [9] and mass transport through the porous electrodes and the membrane (i.e., cross-contamination). Moreover, an effective reactants

distribution is fundamental to enhance electrolyte utilization, that in daily energy storage applications represents up to 40% of VRFB investment cost [10,11]. In fact, increased overpotentials due to mass transport losses lead the battery to reach the operating voltage limits earlier, thus reducing the exchanged capacity during a charge-discharge cycle.

Depending on the nominal operating conditions and electrode morphology, the flow field design results from the trade-off among reduced pressure drops, high efficiency and enhanced electrolyte utilisation. Arenas et al. [12] presented a comprehensive review summarizing flow batteries design requirements and features with particular attention to engineering aspects. The geometry of the flow field was found to be one of the most critical design aspects, since it determines the electrolyte flow through the electrode having an important effect on mass transport conditions.

The literature presents different studies on flow field modifications in VRFBs [13–16]. Houser et al. [13] proposed an equal path length flow field architecture, leading to more net energy discharged, in spite of a substantially larger pressure drop. The developed architecture was evaluated in a 9 cm^2 cell and was effective for cell operating at high current density. Lisboa et al. [14] designed a novel corrugated channel system to enhance mass transport in miniaturized redox flow batteries. For high concentration conditions, an improvement of up to 102% in net power density was obtained in comparison with straight parallel channels flow field. However, the scale-up of these geometries [13,14] to larger plate would likely not be optimal. With the support of a simplified flow resistance model, Zeng et al. [15] proposed a hierarchical interdigitated flow field composed by primary and secondary branch channels which can be independently designed to lower the pumping loss. Compared to the conventional interdigitated flow field, the hierarchical design permitted to increase the pump-based voltage efficiency by 4.2%, evaluated at 240 mA cm^{-2} in a cell with 40 cm^2 active area. Akuzum et al. [16] investigated the effect of varying channel depth with 3D-printed ramps and analysed the

addition of prismatic channel obstructions. Integration of ramps along the channels of interdigitated flow field resulted in 15% increase of peak power density and 40% decrease of pressure drop. However, further investigations would be necessary to better understand the underlying physical phenomena. Brown et al. [17,18] proposed turbulence promoters in form of polymeric meshes within the electrode channels to improve performance in electrochemical systems adopting planar flow-by electrodes. These meshes increase the mean linear electrolyte velocity, resulting in lower electrolyte mass transport resistance, and maintain a uniform gap between membrane and electrodes. However, the concept of turbulence promoters was not exploited for VRFB technology adopting 3D porous electrodes [19].

All these works [13–16] evaluated flow field improvements on battery performance, but the effects of flow field modifications on local region of cell active area was not analysed. In fact, the operation of VRFB is regulated by a complex interplay between kinetic and mass transport phenomena occurring at different scales with a different intensity throughout cell active area. For this reason, a better comprehension of the involved phenomena is fundamental to effectively design improved flow fields. One powerful tool to achieve this objective is computational fluid dynamics (CFD) modelling [20], which allows flexible simulations of system operation varying operating conditions and cell architecture. CFD simulations, when coupled with a rigorous and extensive experimental validation, are able to provide reliable estimations on the distribution of physical quantities, such as reaction rates, velocities and concentrations, and represent a useful tool to aid the flow field design before the manufacturing process [12].

In the literature, different CFD models have been developed for VRFB [21–29], but most of them [21–26] adopt simplified flow field geometries. Oh et al. [21] presented a 3D non-isothermal and transient model considering a simple straight geometry without any channel. In Ma at al. [22], a 3D stationary isothermal model of the negative electrode, with a simple flow through

geometry, highlighted the impact of reactants distribution on the distribution of overpotential, concentrations and current density. Also Wang and Cho [23] developed a 3D dynamic non-isothermal model, in which the model domain was composed of current collectors, electrodes, and a membrane, with no channels. Chen et al. [24] built a 3D transient model with parallel flow field configuration: the fluid dynamics of the flow was carefully investigated, but simulated performance was not compared with experiments. Ozgoli et al. [25] developed a 3D model to evaluate the fluid dynamic behaviour inside porous electrodes, analysing different inlet/outlet configurations in order to determine the best trade-off between performance and pressure drop. However, model validation was not performed. A 3D model was also applied in [26] to study the thermal management of the battery in different operating conditions of current density and flow rate. The approach presented in these works [21–26] allows a better understanding of kinetic and mass transport phenomena regulating VRFB operation, but the adoption of simplified geometries does not permit to correctly estimate *under-the-rib* fluxes and realistic pressure drops.

The state of the art for CFD modelling of VRFBs is represented by [27–29]. Yin et al. [27] simulated a reduced geometry with an interdigitated flow field configuration and the results were validated with respect to a charge/discharge cycle at 60 mA cm^{-2}. Xu et al. [28] developed a 3D model considering a cell without a flow field, with serpentine distributor and with parallel geometry. The different configurations were analysed in terms of performance, overpotentials and pressure drops, but model predictions were only validated with respect to battery performance without a flow field during a charge/discharge cycle at 40 mA cm^{-2}. In [29], the authors developed a 3D CFD model of a 25 cm^2 VRFB in half-cell configuration, simulating the influence of both serpentine and interdigitated flow field. Model results were extensively and rigorously validated with respect to experiments in different operating conditions and with both flow field configurations, providing a more reliable quantification of the involved physical

phenomena. Model simulations evidenced that both flow fields experienced local reactants starvation, with a negative impact on battery performance. For this reason, model validation with respect to current measurements at local level would improve model capabilities to predict battery performance and rationalize the effect of operating conditions. All the model presented in the literature [21–25,27–29] do not consider the verification of heterogeneous operation throughout cell active area, that has been already characterized experimentally in different segmented single cell hardware [30–34].

In [35], the authors characterized VRFB local operation in the same experimental set-up used in this work, demonstrating that VFRB performance is strongly heterogeneous and the adopted flow field plays a key role in the definition of current density distribution. Therefore, also local characterization is fundamental to provide a better understanding of the distribution of the electrolyte over the porous electrode.

This work presents the design of improved flow fields with the aid of a 3D VRFB model, that has been validated for the first time in the literature with respect to local polarization curves collected on a segmented cell hardware [35], adopting both serpentine and interdigitated flow fields. Each operating condition and flow field geometry is represented simultaneously by 10 different local polarization curves. The 3D model is based on the VRFB half-cell model already described in [29] that in this work has been integrated in order to simulate a VRFB in symmetric cell configuration with both positive and negative electrolyte. Improved flow fields, that are based on an interdigitated-like distributor with the introduction of channel obstructions, are subsequently tested and compared with conventional interdigitated and serpentine geometries, in terms of performance, pressure drops and exchanged capacity during cycling operation. Moreover, the effect of flow field modifications is also evaluated with respect to local current density distribution, permitting a better understanding of the underlying physical phenomena.

The work is organised as follows: the experimental hardware and tests are described in Section 2, and then, in Section 3 model development is presented. Section 4 firstly presents model validation and its application to design channel obstructions; subsequently experimental results are presented, highlighting obstructions effect on local performance. Finally, some conclusions are given in Section 5.

2. Experimental

2.1 Experimental setup

The local performance characterization was performed with the macro-segmented flow battery (m-SFB) developed and described in [35]. The adopted m-SFB featured segmentation in 10 electrically insulated macro-regions at both flow fields and current collectors, while no modifications of electrodes were required. Flow-plates were developed and manufactured in-house, with the 10 macro-regions held together by means of a 0.8 mm layer of insulating inert epoxy resin [35]. Single serpentine and interdigitated geometry were adopted and considered as benchmark distributors, while for innovative geometries an *ad-hoc* flow field was designed and manufactured (Fig. 1). It was based on the concept of interdigitated flow-field, permitting the positioning of different inserts in four different locations along the x-direction of the distributor (highlighted in Fig.1). For the sake of simplicity Fig. 1 illustrates the developed hardware coupled with inserts named “0”, that reproduce the interdigitated geometry (i.e., no obstructions in the channels). The other insert typologies, named “1” and “2”, were designed with the aid of CFD model and are described later on in this work (Section 4.2). The developed hardware permits thus to realize and test multiple flow field configurations, varying the number and/or typology of the inserts. The nomenclature used to identify the innovative flow-

field geometry consists in 4 digits indicating the typology of the adopted insert for each of the four locations in the x-direction of the distributor, ranging from electrolyte inlet to outlet[1].

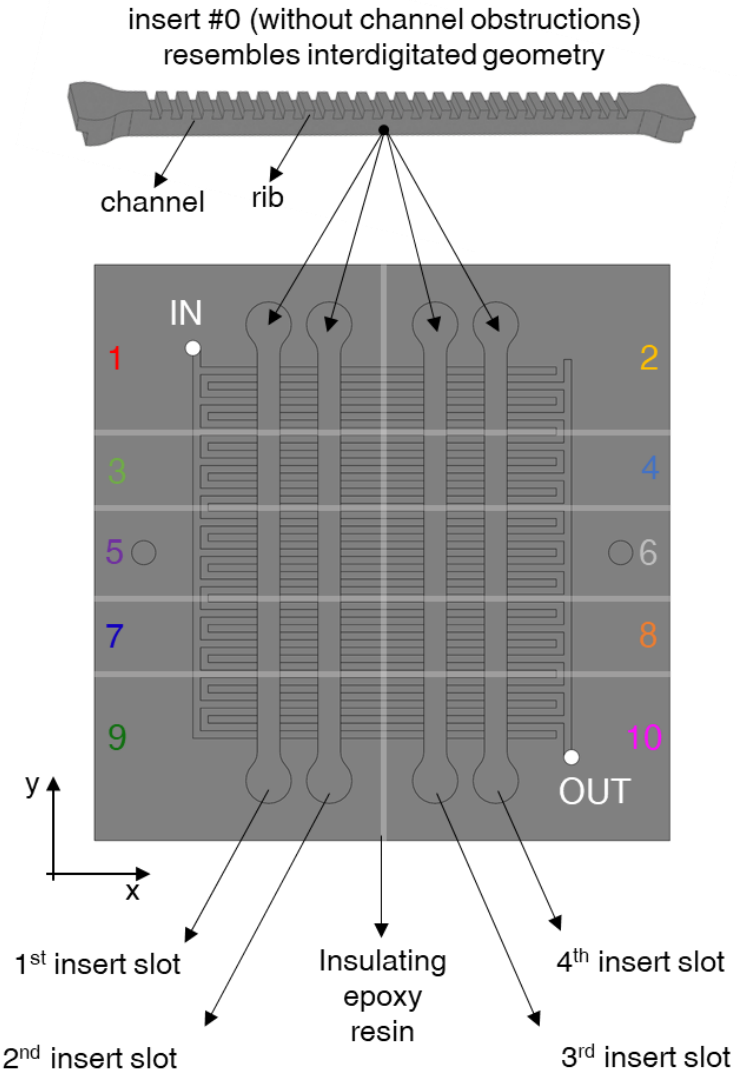

Fig. 1 – Ad-hoc flow field for innovative geometries with inserts #0.

Since inserts made in graphite guarantee electric contact between the different macro-regions of the distributor (highlighted and numbered in Fig. 1), in a first phase they were realized in Teflon™ in order to maintain spatial resolution of current density and investigate the effect of

[1] In example, the notation 1-0-0-0 indicates that insert #1, which is characterized by channel obstructions type #1 in all the feeding channels, is placed only in the first slot close to electrolyte inlet (at 2.3 cm of the x-coordinate); while insert #0 is present in all the other insert slots. The notation 0-0-0-2 indicates that insert #2, which is characterized by channel obstructions type #2 in all the feeding channels, is placed just in the last slot close to electrolyte outlet (at 5.3 cm of x-coordinate); while insert #0 is present in all the other insert slots.

inserts on local battery performance[2]. The presence of Teflon™ reduces the electric contact between electrode and flow plates with a consequent decrease of overall battery performance. However, all the tests were also repeated with inserts made in graphite in order to quantify their effect on overall battery performance[3].

Ten high-precision source-measure units (SMU) modules (NI PXIe- 4139) were used to control the operation of each macro-region and measure local polarization curves. The m-SFB operation was potentiostatic: being all the macro-regions at same voltage avoids the occurrence of internal cross-currents [35].

The cell active area was 25 cm^2. Both positive and negative electrodes were untreated Sigracet® 39AA (nominal thickness of ~280 μm [36], compressed to 230 μm), while the membrane was Nafion™ 115 (thickness 127 μm). The cell was maintained at a room temperature of 21±2 °C.

Positive and negative electrolytes were aqueous solutions of vanadium ions and 5 M sulfuric acid (Fischer Chemicals), prepared starting from vanadium IV sulfate oxide hydrate (Alfa Aesar) following the procedure described in [37]. In order to avoid the intake of air, the bottles containing the electrolyte were pressurized with N_2. The positive and negative electrolytes were fed to the battery through a peristaltic pump (Watson-Marlow 323Du with a 4-roller head pump). In the hydraulic circuit a pressure transducer (Druck PMP1400, accuracy ±0.15% of pressure) was utilised to measure the pressure loss between the cell inlet and outlet.

2.2 Experimental tests

2.2.1 Polarization curves

Polarization curves were performed at 50% state of charge (SoC) in symmetric cell configuration using both positive (VO_2^+/VO^{2+}) and negative (V^{2+}/V^{3+}) electrolyte. It has to be

[2] If the insert is made in a conductive material, the local measurement of current won't be possible due to the electric contact between the different macro-regions of the cell active area.

[3] The material of inserts has been specified in all the figures legends. When graphite is used it is not possible to perform local measurements of current density.

remarked that the symmetric cell configuration permits to maintain a constant SoC during the test due to the absence of cross-contamination effects [38]: the choice of this configuration was given by the considerably high number of tests performed, varying the operating conditions and the flow field configuration. In fact, polarization curves in full cell configuration[4] are affected by cross-contamination of the electrolytes and a small difference in battery performance could be mitigated by a not ideal management of electrolytes SoC and concentration. Moreover, in [35] it was demonstrated that polarization curves in symmetric cell configurations are representative of the operation in full cell, which is mainly regulated by the performance of the negative electrode (considering the adopted operating conditions and electrode material).

Vanadium concentration was 1.6 M and each electrolyte volume was 300 ml. The following voltage ranges were adopted: 0.5/-0.5 V for the symmetric cell with positive electrolyte and 0.35/-0.35 V for symmetric cell with negative electrolyte. Voltage limits were prescribed in order to avoid the occurrence of undesired side reactions, such as hydrogen and/or oxygen evolution. Voltage steps of 0.05 V were applied and each voltage value was held for 120 s in order to reach a steady-state condition. All the tests have been performed at different flow rates, ranging from 15 to 90 ml min^{-1} depending on the adopted flow field and electrolyte. Further details on segmented cell hardware and post processing of raw data are reported in [35].

2.2.2 Charge-discharge cycles

In order to evaluate the battery performance in full cell configuration and monitor the evolution of exchanged capacity as a function of the adopted flow field, 60 charge-discharge cycles at 40

[4] In full cell configuration V^{2+}/V^{3+} electrolyte is fed at the negative electrode, while VO_2^+/VO^{2+} electrolyte is fed at the positive electrode.

ml min^{-1} were performed at 0.1 A cm^{-2} and 0.2 A cm^{-2}, imposing 1.1 V and 1.8 V as lower and upper voltage limits [39], respectively. Vanadium concentration was 1 M and the electrolyte volume was 100 ml: the resulting ideal battery capacity was 2.68 Ah. Fresh electrolyte solutions were used for each series of cycle.

3. Model

3.1 Model development and assumptions

A custom model of a VRFB was developed with the aid of a commercial fluid dynamics code (ANSYS Fluent 18). The model couples fluid dynamics and electrochemistry and simulates VRFB performance in full cell and symmetric cell configurations. The model domain with serpentine and interdigitated flow fields is illustrated in Fig. A1A and A1B, respectively. It replicates the 25 cm^2 experimental hardware and is composed of a 1 mm x 1 mm distributor channel (D_1, D_5), which feeds the electrolyte over a 230 μm-thick (compressed thickness) porous carbon electrode (D_2, D_4). A 127 μm thick polymer membrane (D_3) separates the two electrodes and allows proton transport. These different domains are highlighted in Fig. A1C.

The main electrochemical reactions occurring at the negative and positive electrode during nominal battery operation are, respectively:

$$V^{2+} \underset{charge}{\overset{discharge}{\rightleftharpoons}} V^{3+} + e^- , \qquad E_{eq} = -0.255\ V\ vs\ SHE \qquad \text{(I)}$$

$$VO_2^+ + 2H^+ + e^- \underset{charge}{\overset{discharge}{\rightleftharpoons}} VO^{2+} + H_2O , \qquad E_{eq} = 1.004\ V\ vs\ SHE \qquad \text{(II)}$$

When symmetric cell configuration with positive or negative electrolyte is modelled, the corresponding electrolyte reaction is imposed at both electrodes: for negative voltage, discharge and charge occur at the negative and positive electrode, respectively.

As reported in [29], the model neglects the dissociation rate of sulphuric acid [23], considering a complete first step of dissociation of H_2SO_4 into HSO_4^- and H^+, and the equilibrium of the

second step of dissociation of HSO_4^- into H^+ and SO_4^{2-}, whose concentration remains therefore constant (except for H^+, since involved in vanadium redox reactions). The main model assumptions are the following:

- The model is stationary and isothermal.
- The electrolyte is incompressible.
- The flow regime is laminar, because of the limited velocities expected from the simulated flow rates. The assumption is verified a posteriori analysing the simulated velocity field.
- Electrodes and membrane properties are isotropic.
- Electrolyte physical properties are not dependent on the SoC. This assumption is frequently adopted in the literature [23,24,29]. Moreover, in this work just symmetric cell is modelled and considering the adopted reactants stoichiometry the variation of SoC along the distribution channels is limited.
- Membrane is not permeable to vanadium ions.
- Electroneutrality principle of the electrolytes is assumed. This hypothesis allows to compute the concentration profile for one species, without the resolution of the corresponding species balance equation [40].

3.2 Mass balance

The conservation of mass was computed through continuity equation in all model domains except for the membrane (D_1, D_2, D_4, D_5):

$$\rho \nabla \cdot \boldsymbol{u} = 0 \tag{1}$$

where ρ is the electrolyte density and $\boldsymbol{u}$ the velocity.

3.3 Momentum balance

In order to guarantee a smooth transition of the velocity profile between channel and electrode, Navier-Stokes equation for momentum conservation (Eq. 2) and Brinkmann equation (Eq. 3) were used to compute the conservation of momentum in the channels (D_1, D_5) and in the porous electrodes (D_2, D_4), respectively:

$$\nabla \cdot (\rho \boldsymbol{u}\boldsymbol{u}) = -\nabla p + \nabla \cdot \left[\mu \left(\nabla \boldsymbol{u} + (\nabla \boldsymbol{u})^T \right) \right] + \boldsymbol{f} \quad (2)$$

$$\frac{1}{\varepsilon^2} \nabla \cdot (\rho \boldsymbol{u}\boldsymbol{u}) = -\nabla p + \nabla \cdot \left[\frac{\mu}{\varepsilon} \left(\nabla \boldsymbol{u} + (\nabla \boldsymbol{u})^T \right) \right] - \frac{2\mu}{3\varepsilon} \nabla (\nabla \cdot \boldsymbol{u}) - \left(\frac{\mu}{\kappa} + \beta_F |\boldsymbol{u}| + S_m \right) \boldsymbol{u} + \boldsymbol{f} \quad (3)$$

where ε is the porosity of the compressed porous electrode[5], p is the pressure, μ the dynamic viscosity of the fluid, κ the permeability of the porous electrode. β_F is the Forchheimer drag coefficient, which was neglected in the present work, and $\boldsymbol{f}$ is the volume force vector, which is zero as gravity is not considered.

3.4 Species balance

The conservation of each species was solved according to (Eq. 4):

$$\nabla \cdot \boldsymbol{N}_i = S_i \quad (4)$$

where S_i is the species molar source, that depends on the reaction rate of the electrochemical reactions and on the simulated cell configuration (Section 3.5). The molar flux $\boldsymbol{N}_i$ was described with the Nernst-Planck equation (Eq. 5), in which the molar flux of each species is regulated by three transport mechanisms: diffusion, migration and convection.

$$\boldsymbol{N}_i = -D_i^{eff} \nabla c_i - z_i u_i c_i F \nabla \phi_l + \boldsymbol{u} c_i \quad (5)$$

[5] The porosity value of the compressed electrode is calculated reducing the void volume of the electrode by the compression ratio of about 20%, while the volume occupied by the incompressible carbon fibres is kept unaltered. [34]

D_i^{eff} is the effective diffusivity, c_i is the molar concentration, z_i is the charge number, u_i is the mobility calculated according to the Nernst-Einstein equation and ϕ_l is the potential of the liquid phase. The Nernst-Plank equation was not solved for SO_4^{2-} as a result of the electroneutrality principle:

$$\sum_i z_i c_i = 0 \tag{6}$$

The effective diffusivity was obtained according to the Bruggeman correction [29].

The membrane was considered permeable to only protons and the electrolytic potential was solved as discussed in Section 3.5.

3.5 Charge balance

Charge conservation (Eq. 7) was solved in all the domains, imposing a non-zero source term i_R only in the porous electrodes (D_2, D_4).

$$\nabla \cdot \boldsymbol{i}_l = -\nabla \cdot \boldsymbol{i}_s = i_R \tag{7}$$

$\boldsymbol{i}_s$ is the current density in the solid phase and $\boldsymbol{i}_l$ is the current density in the liquid electrolyte phase, given by:

$$\boldsymbol{i}_s = -\sigma_s^{eff} \nabla \phi_s \tag{8}$$

$$\boldsymbol{i}_l = F \sum_i z_i \boldsymbol{N}_i = F \sum_i z_i \left(-D_i^{eff} \nabla c_i - z_i u_i c_i F \nabla \phi_l + \boldsymbol{u} c_i \right) \quad \text{(in electrolyte)} \tag{9}$$

$$\boldsymbol{i}_l = -\sigma_l \nabla \phi_l \quad \text{(in membrane)} \tag{10}$$

$\sigma_s^{eff} = (1-\varepsilon)^{3/2} \sigma_s$ is the effective electric conductivity of the solid phase and σ_l is the membrane protonic conductivity.

The source term i_R in the porous electrodes for both redox couples is expressed by Butler-Volmer kinetics:

$$i_R^{II-III} = k_0^{II-III} a^{II-III} F \left(c_{V^{2+}}^s \cdot e^{\frac{\alpha^{II-III} F \eta^{*,II-III}}{RT}} - c_{V^{3+}}^s \cdot e^{-\frac{\left(1-\alpha^{II-III}\right) F \eta^{*,II-III}}{RT}} \right) \quad (11)$$

$$i_R^{IV-V} = k_0^{IV-V} a^{IV-V} F \left(c_{VO^{2+}}^s \cdot e^{\frac{\alpha^{IV-V} F \eta^{*,IV-V}}{RT}} - c_{VO_2^+}^s \cdot e^{-\frac{\left(1-\alpha^{IV-V}\right) F \eta^{*,IV-V}}{RT}} \right) \quad (12)$$

where k_0 is the reaction rate constant, a is the specific surface area, α is the charge transfer coefficient, T is the temperature and the c_i^s terms are the concentrations of vanadium ions on the surface of the electrode. The overpotential η^* is defined as:

$$\eta^* = \varphi_s - \varphi_l - E_{eq} \quad (13)$$

where E_{eq} is the equilibrium potential for the considered reaction. As reported in [29], the concentration of vanadium ions on the surface of the electrode is calculated from the bulk concentration using a convective mass transport model with a mass transport coefficient h_m obtained according to the correlation reported in [41]. The resulting source terms as a function of the bulk concentrations result in:

$$i_R^{II-III} = \frac{k_0^{II-III} a^{II-III} F}{1 + \frac{k_0^{II-III}}{h_m^{II-III}} \cdot \left(e^{\frac{\alpha^{II-III} F \eta^{*,II-III}}{RT}} + e^{-\frac{(1-\alpha^{II-III}) F \eta^{*,II-III}}{RT}} \right)} \left(c_{V^{2+}}^b \cdot e^{\frac{\alpha^{II-III} F \eta^{*,II-III}}{RT}} - c_{V^{3+}}^b \cdot e^{-\frac{(1-\alpha^{II-III}) F \eta^{*,II-III}}{RT}} \right) \quad (14)$$

$$i_R^{IV-V} = \frac{k_0^{IV-V} a^{IV-V} F}{1 + \frac{k_0^{IV-V}}{h_m^{IV-V}} \cdot \left(e^{\frac{\alpha^{IV-V} F \eta^{*,IV-V}}{RT}} + e^{-\frac{(1-\alpha^{IV-V}) F \eta^{*,IV-V}}{RT}} \right)} \left(c_{VO^{2+}}^b \cdot e^{\frac{\alpha^{IV-V} F \eta^{*,IV-V}}{RT}} - c_{VO_2^+}^b \cdot e^{-\frac{(1-\alpha^{IV-V}) F \eta^{*,IV-V}}{RT}} \right) \quad (15)$$

Table 1[6] reports the values of the species molar source S_i (Eq. 4) for both positive and negative electrode as a function of the simulated cell configurations.

[6] In symmetric cell configuration, when a negative voltage is applied to the battery, discharge and charge occur at the negative and positive electrode, respectively. Therefore i_R^{II-III} is positive (negative) at the negative (positive) electrode, while i_R^{IV-V} is negative (positive) at the negative (positive) electrode.

Table 1 – Species molar source S_i for both positive and negative electrode as a function of the simulated cell configurations.

	Symmetric cell with negative electrolyte		Symmetric cell with positive electrolyte	
	Negative electrode	Positive electrode	Negative electrode	Positive electrode
$S_{V^{2+}}$	$-i_R^{II-III}/F$	$-i_R^{II-III}/F$	-	-
$S_{V^{3+}}$	i_R^{II-III}/F	i_R^{II-III}/F	-	-
$S_{VO^{2+}}$	-	-	$-i_R^{IV-V}/F$	$-i_R^{IV-V}/F$
$S_{VO_2^+}$	-	-	i_R^{IV-V}/F	i_R^{IV-V}/F
S_{H^+}	-	-	$2i_R^{IV-V}/F$	$2i_R^{IV-V}/F$

3.6 Boundary conditions

At the inlet of the distributor channel, the mass fraction of each species was set along with a uniform flow velocity value depending on the chosen volumetric flow rate. The values of velocity and concentrations of species at the outlet of negative electrode were set as boundary conditions at the inlet of positive electrode. Table 2 reports the values of concentrations set as boundary conditions[7] for both positive and negative electrodes as a function of the simulated cell configurations.

Table 2 – Boundary conditions on ions concentration for both positive and negative electrode as a function of the simulated cell configurations.

	Symmetric cell with negative electrolyte		Symmetric cell with positive electrolyte	
	Negative electrode	Positive electrode	Negative electrode	Positive electrode
$c_{V^{2+}}$	$SoC^{II-III} \cdot M_V$	$SoC_{out,-}^{II-III} \cdot M_V$	-	-
$c_{V^{3+}}$	$\left(1-SoC^{II-III}\right)\cdot M_V$	$\left(1-SoC_{out,-}^{II-III}\right)\cdot M_V$	-	-
$c_{VO^{2+}}$	-	-	$\left(1-SoC^{IV-V}\right)\cdot M_V$	$\left(1-SoC_{out,-}^{IV-V}\right)\cdot M_V$
$c_{VO_2^+}$	-	-	$SoC^{IV-V} \cdot M_V$	$SoC_{out,-}^{IV-V} \cdot M_V$
c_{H^+}	M_{acid}	M_{acid}	$M_{acid} - C_{VO^{2+}}$	$M_{acid} - C_{VO^{2+}out,-}$
$c_{HSO_4^-}$	$M_{acid} + M_V$	$M_{acid} + M_V$	$M_{acid} + M_V$	$M_{acid} + M_V$

[7] All the quantities with 'out' subscript are obtained from the values at channel outlet of the negative electrode and are consequently dependent on the simulated operating condition. All the other numerical values used for the simulations are reported in Table 3.

$c_{SO_4^{2-}}$	$M_{acid} - M_V$	$M_{acid} - M_V$	$M_{acid} - M_V$	$M_{acid} - M_V$

The pressure gauge value was set to zero as a reference at the outlet of the positive electrode and pressure values obtained at the inlet of the positive electrode were set as boundary conditions at the outlet of the negative electrode.

The electric potential on the contact areas between the electrode and the current collector (not present in the computational domain) was set according to the working point selected for the simulation at the negative electrode, while at the positive electrode the electric potential was set to be the electric ground. Regarding the electrolytic potential, the boundary conditions were set to null flux on the abovementioned surfaces. The interfaces between the membrane and the porous electrodes were set not permeable to all chemical species and electrons, and the continuity of the electric potential and its flux is ensured. All the remaining boundaries were considered impermeable to all physical quantities.

3.7 Software setup and mesh analysis

The model was implemented in the commercial code ANSYS® Fluent 18 adopting custom user defined functions (UDFs) for the description of electrochemistry, together with the standard fluid dynamics module. The solver used a SIMPLE algorithm for the pressure-velocity coupling, a PRESTO! scheme for the resolution of pressure and a second order upwind scheme for the discretisation of the remaining equations.

The mesh employed for all the investigated flow field configurations was a hexahedral structured mesh, refined for the sake of accuracy in the porous electrode and in specific zones of the channels, where higher gradients are expected. Moreover, in order to assure the independency of the solutions from the spatial discretization, an analysis of the *Grid Convergence Index* (GCI) for different quantities was carried out using a finer and a coarser grid. The analysis exhibited an error band lower than 1% with respect to the asymptotic solution for

all the investigated geometries. This error band could be reduced with further refinements of the mesh, but this would increase the time required for the simulations.

4. Results and discussion

4.1 Model validation

Fig. 2A-D reports the comparison between simulated and measured local polarization curves for both serpentine (Fig. 2A-B) and interdigitated (Fig. 2C-D) flow fields. The model has been calibrated with respect to local data in symmetric cell configuration[8] at 20 ml min^{-1}, condition in which the differences among the local current density measurements are exacerbated [35]. The model calibration with respect to experimental data in symmetric cell permits to eliminate the effect of electrolyte imbalance due to cross-contamination and to limit the number of fitting parameters for each experiment, reducing the uncertainty in their evaluation. Just kinetic constant of negative and positive electrode, electrode permeability, electrode active area, and convective mass transport coefficient inside pores were fitted, while all the other parameters were assumed. The assumed and fitted model parameters are reported in Table 3. Due to the high computational time of simulations, the fitting parameters were changed without the aid of already *built-in* fitting procedures. Model calibration was an iterative and time expensive process and it required a preliminary sensitivity analysis on the effect of model parameters (not reported for the sake of brevity). For both flow fields the model parameters were kept constant: a better agreement between model and experiments could be obtained varying the fitting parameters between serpentine and interdigitated simulations, but this is out of the scope of this work. On the contrary, the different flow field configuration was extremely important for

[8] Since at SoC 50% the performance is symmetric, only the data with positive current density and negative voltage values are reported.

model calibration since electrolyte distribution, velocities and pressure drops are considerably different between the two geometries.

In particular, mass transport related parameters (electrode permeability and convective mass transport coefficient) were calibrated with respect to experimental data of symmetric cell with positive electrolyte[9], since its operation is not limited by kinetic losses and shows a typical mass transport dominated behaviour towards high operating current [35]. Instead, the operation of symmetric cell with negative electrolyte is strongly affected by the sluggish electrode kinetic and the effect of mass transport parameters is less relevant considering the limited range of operating current. Moreover, there is a complex interplay among the fitted model parameters: once the permeability is fixed, the kinetic constant mainly defines the overall performance, but the local ones are strongly affected by the specific active area and convective mass transport coefficient in the electrode pores. The former affects the magnitude of local flux in the pores, while the latter, that is dependent on electrolyte velocity, defines local mass transport losses in the pores. Considering that the model has been calibrated also with respect to local polarization curves (11 polarization curves for each operating condition and flow field configuration, corresponding to 77 experimental points), the number of fitting parameters can be considered acceptable and the resulting numerical values are defined with a reduced uncertainty.

[9] Two different numerical values of convective mass transport coefficient are reported in Table 3. The correlation used for its estimation [41] ($Sh = \mathcal{A} Re^{0.4}$) is the same for both electrolytes, in which $\mathcal{A}$ is a constant that is fitted with respect to experimental data of symmetric cell with positive electrolyte. The fitting parameter $\mathcal{A}$ is necessary since the correlation reported in [41] has been obtained for a simplified geometry consisting of a single electrode fibre. Considering that electrolyte diffusivity and viscosity present in Reynolds and Sherwood numbers are different between positive and negative electrolyte, once the convective mass transport coefficient of the positive electrolyte (h_m^{IV-V}) is defined, the corresponding one at the negative electrode results equal to: $h_m^{II-III} = \frac{D_{V^{2+}/V^{3+}}}{D_{VO^{2+}/VO_2^+}} \left(\frac{\mu^{IV-V}}{\mu^{II-III}} \right)^{0.4} h_m^{IV-V} = 0.631 \cdot h_m^{IV-V}$.

Table 3 – Assumed and fitted model parameters.

Symbol	Description	Value	Unit	Reference
E_{eq}^{IV-V}	Positive electrode equilibrium potential	1.004	V	-
E_{eq}^{II-III}	Negative electrode equilibrium potential	−0.255	V	-
F	Faraday constant	96485	C mol^{-1}	-
R	Universal gas constant	8.314	J mol^{-1} K^{-1}	-
T	Temperature	300	K	-
$D_{V^{2+}}$	V^{2+} diffusivity	$2.4 \cdot 10^{-10}$	m^2 s^{-1}	[42]
$D_{V^{3+}}$	V^{3+} diffusivity	$2.4 \cdot 10^{-10}$	m^2 s^{-1}	[42]
$D_{VO^{2+}}$	V^{4+} diffusivity	$3.9 \cdot 10^{-10}$	m^2 s^{-1}	[42]
$D_{VO_2^+}$	V^{5+} diffusivity	$3.9 \cdot 10^{-10}$	m^2 s^{-1}	[42]
D_{H^+}	H^+ diffusivity	$9.3 \cdot 10^{-9}$	m^2 s^{-1}	[40]
D_{HSO^-}	HSO^- diffusivity	$1.33 \cdot 10^{-9}$	m^2 s^{-1}	[40]
$D_{SO^{2-}}$	SO^{2-} diffusivity	$1.065 \cdot 10^{-9}$	m^2 s^{-1}	[40]
$\varepsilon_{\text{no compression}}$	Electrode porosity w/o compression	0.89	-	[36]
ε	Electrode porosity with compression	0.859	-	
a	Specific active area	$8 \cdot 10^4$	m^2 m^{-3}	fitted
ρ	Electrolyte density	1350	kg m^{-3}	measured
μ^{IV-V}	Viscosity of positive electrolyte	$1.32 \cdot 10^{-3}$	Pa s	[43]
μ^{II-III}	Viscosity of negative electrolyte	$1.24 \cdot 10^{-3}$	Pa s	[43]
α^{IV-V}	Transfer coefficient of positive electrode	0.5	-	[38]
α^{II-III}	Transfer coefficient of negative electrode	0.5	-	[38]
k_0^{IV-V}	Reaction rate of positive electrode	$4.94 \cdot 10^{-6}$	m s^{-1}	fitted
k_0^{II-III}	Reaction rate of negative electrode	$6.2 \cdot 10^{-7}$	m s^{-1}	fitted
κ	Electrode permeability	$6.67 \cdot 10^{-11}$	m^2	fitted
h_m^{IV-V}	Convective mass transport coefficient at positive electrode	$2.5 \cdot 10^{-4} \cdot \boldsymbol{u}^{0.4}$	-	fitted
h_m^{II-III}	Convective mass transport coefficient at negative electrode	$1.6 \cdot 10^{-5} \cdot \boldsymbol{u}^{0.4}$	-	fitted
σ_l	Electrolyte conductivity	3	S m^{-1}	measured
σ_s	Electrode conductivity	5	S m^{-1}	[36]
M_V	Vanadium molarity in the electrolyte	1.6	mol l^{-1}	-
M_{acid}	Sulfuric acid molarity	5	mol l^{-1}	-
SoC^{IV-V}	State of charge of positive electrolyte	50	%	-
SoC^{II-III}	State of charge of positive electrolyte	50	%	-

It is worth noting that the model reproduces experiments with acceptable accuracy at local level (Fig. 2A-D), confirming that it well describes the distribution of reaction rate across cell active area: this is a very important feature and it is fundamental in order to use the model to support

the design of innovative distributors. Average deviations from experimental current densities of 24 mA cm^{-2} and 36 mA cm^{-2} are obtained for serpentine with positive and negative electrolyte respectively, while for the interdigitated distributor the values are respectively 35 mA cm^{-2} and 21 mA cm^{-2}.

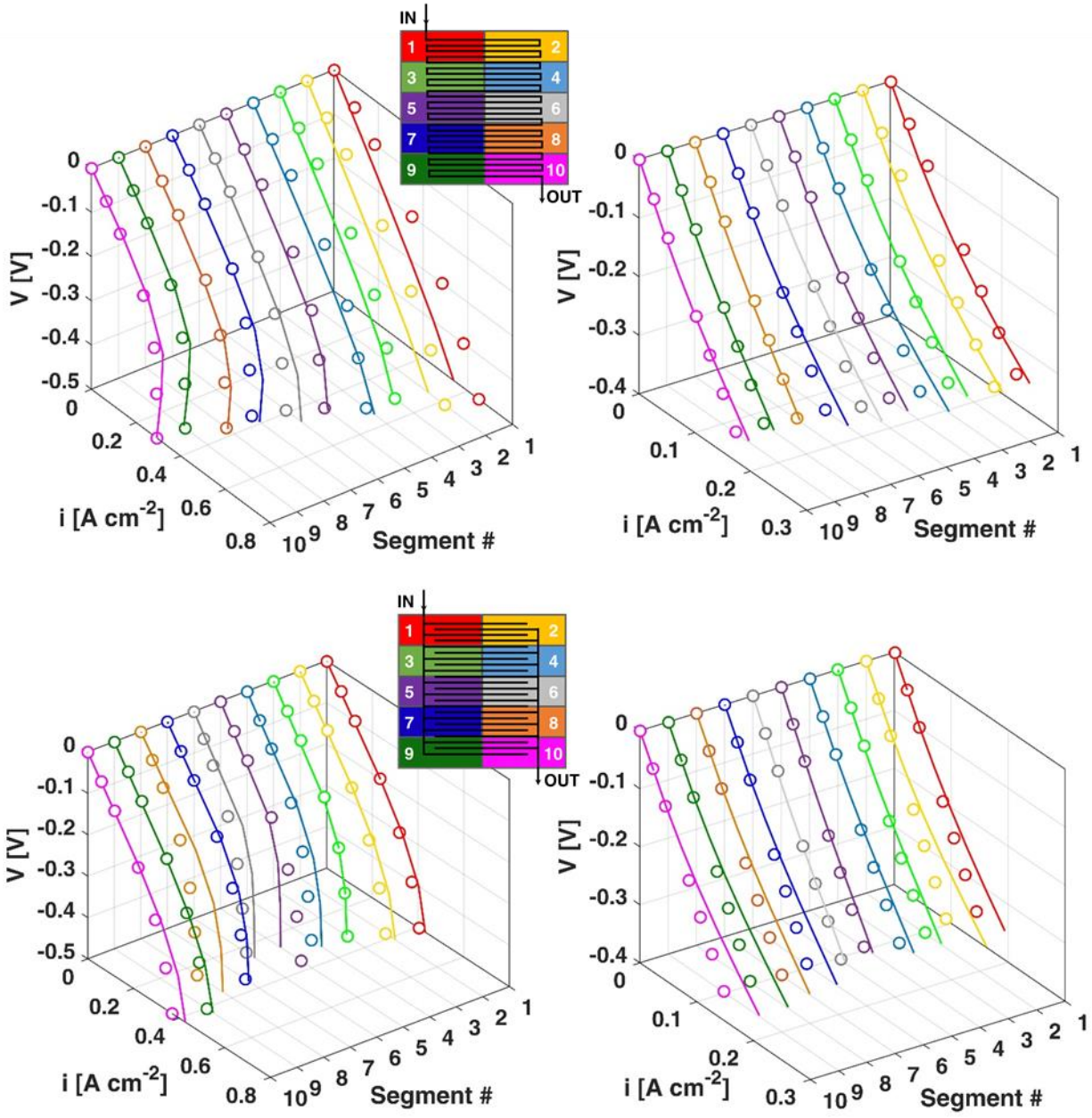

Fig. 2 – Comparison between simulated (solid lines) and experimental (dots) local polarization curves at 20 ml min^{-1}: A) positive electrolyte with serpentine; B) negative electrolyte with serpentine; C) positive electrolyte with interdigitated; D) negative electrolyte with interdigitated. Reactants stoichiometry at 20 ml min^{-1} and 0.2 A cm^{-2} is around 5.

Moreover, the model was validated according to experiments at higher electrolyte flow rates: Fig. 3 reports the simulated and measured overall battery performance at 20 ml min^{-1} along with the ones at higher flow rates. It is worth noting that model simulations correctly describe the trend of experimental data induced by a higher flow rate with positive and negative electrolyte, considering both interdigitated (Fig. 3A) and serpentine (Fig. 3B) distributor. At 20 ml min^{-1} serpentine presents higher performance compared to interdigitated, but the flow rate increase is more impactful adopting interdigitated geometry.

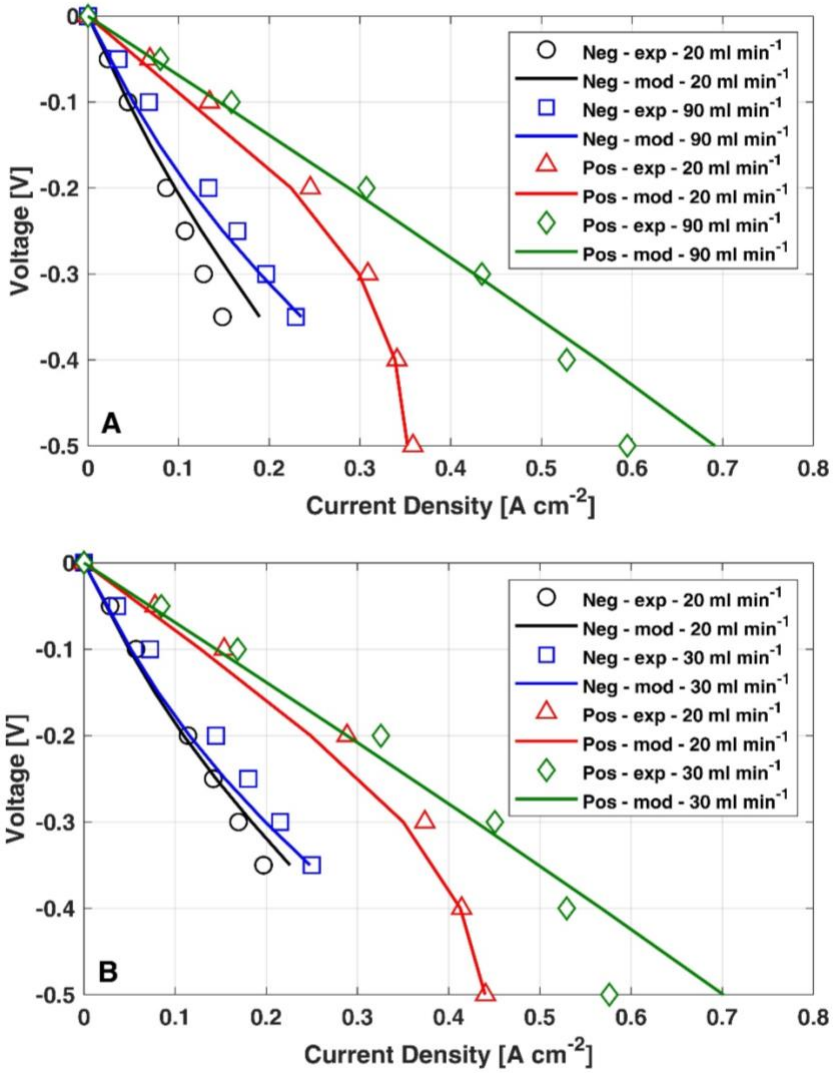

Fig. 3 – Simulated (solid lines) and measured (markers) polarization curves in symmetric cell with positive and negative electrolyte at different flow rates: A) interdigitated; B) serpentine.

As already reported in a previous work by the authors [35], serpentine performs better at channel inlet (Fig. 2A-B), while the interdigitated exhibits poor performance in the middle

region of cell active area (Fig. 2C-D), due to low values of electrolyte velocity in the porous electrode. This behaviour is less evident considering the negative symmetric cell, since its operation is mainly hindered by kinetic losses, resulting in a limited range of operating current. Serpentine and interdigitated flow fields not only present a different current density distribution, but also differ in the value of pressure drops. In the serpentine geometry, the considerably higher electrolyte velocity results in greater pressure drops [44]. As already known in the literature [29], the pressure difference between adjacent channels regulates electrolyte permeation through porous electrode: higher pressure drops enhance the so-called *under-the-rib* fluxes, but on the other hand increases auxiliary consumption. The difference in pressure drops between the two flow fields increases in cells characterized by higher area, exacerbating the impact of auxiliary consumption on the system efficiency for the serpentine. In fact, despite in the investigated operating conditions of this work serpentine exhibits better performance compared to the interdigitated flow field, the considerable higher pressure drops suggest that this geometry is not suitable for cell scale-up[10]. Moreover, considerably higher electrolyte velocities in the porous electrodes could lead to higher ions permeation through the membrane, enhancing electrolyte imbalance due to cross-contamination. However, this phenomenon does not affect battery performance in symmetric cell configuration.

Therefore, the design of improved flow fields needs to consider their possible utilization in a real system and results from a meticulous trade-off between performance, pressure drop and exchanged capacity during cycling, which are regulated by the complex interaction among different electrochemical and mass transport phenomena occurring at local level throughout cell active area.

4.2 Design of channel obstructions

[10] The measured pressure drops are reported later in the text in Fig. 6C.

After an extensive model validation in different operating conditions with respect to experimental data of symmetric cell with both positive and negative electrolyte coupled with serpentine and interdigitated flow fields, the model can be used as a tool to design innovative flow fields. The idea behind the development of improved geometries relies on the fact that serpentine flow field is not suitable for cell scale-up, while the interdigitated one, despite the lower performance, presents limited pressure drops. The innovative geometries developed in this work exploit the operating principle of interdigitated flow field, which is composed of closed-end parallel channels, alternating channels for electrolyte feeding and channels for its discharge. The concept of channel obstruction consists in the introduction of a localized pressure drop just in the feeding channels to promote the pressure difference between feeding and discharge channels, enhancing the *under-the-rib* fluxes (i.e., electrolyte permeation) through the porous electrode. At the same time, the obstruction does not completely occlude feeding channels and permits to part of the electrolyte to flow along it.

During the design of channel obstructions, simulations were not performed considering the 25 cm^2 active area of the battery, but the model domain was reduced to a pair of feeding and discharge channels with a length of 5 cm each. Considering channel dimension (1 mm x 1 mm) and the manufacturing capabilities, two different channel obstructions were designed and both obstructs 50% of channel section: the first one (named #1) is located at the channel wall (Fig. 4A2), while the second one (named #2) is placed close to electrode interface (Fig. 4A3). In Fig. 4A1 the standard interdigitated is reported as the benchmark configuration. Both obstructions have a dimension of 3 mm in the direction of electrolyte flow in the channel. The highlighted planes in Fig. 4A represent the locations of physical quantities illustrated in Fig. B, C, D, that reports model simulations of two consecutive channels.

The main difference between the two obstructions is evident in the fluid flow (Fig. 4B): while in correspondence of the obstruction the #1 forces a higher share of electrolyte to permeate

through the porous electrode (Fig. 4B2), reducing the fraction continuing to flow along the channel, the #2 better allows a relevant part of the electrolyte to flow towards the channel end with a greater velocity (Fig. 4B3).

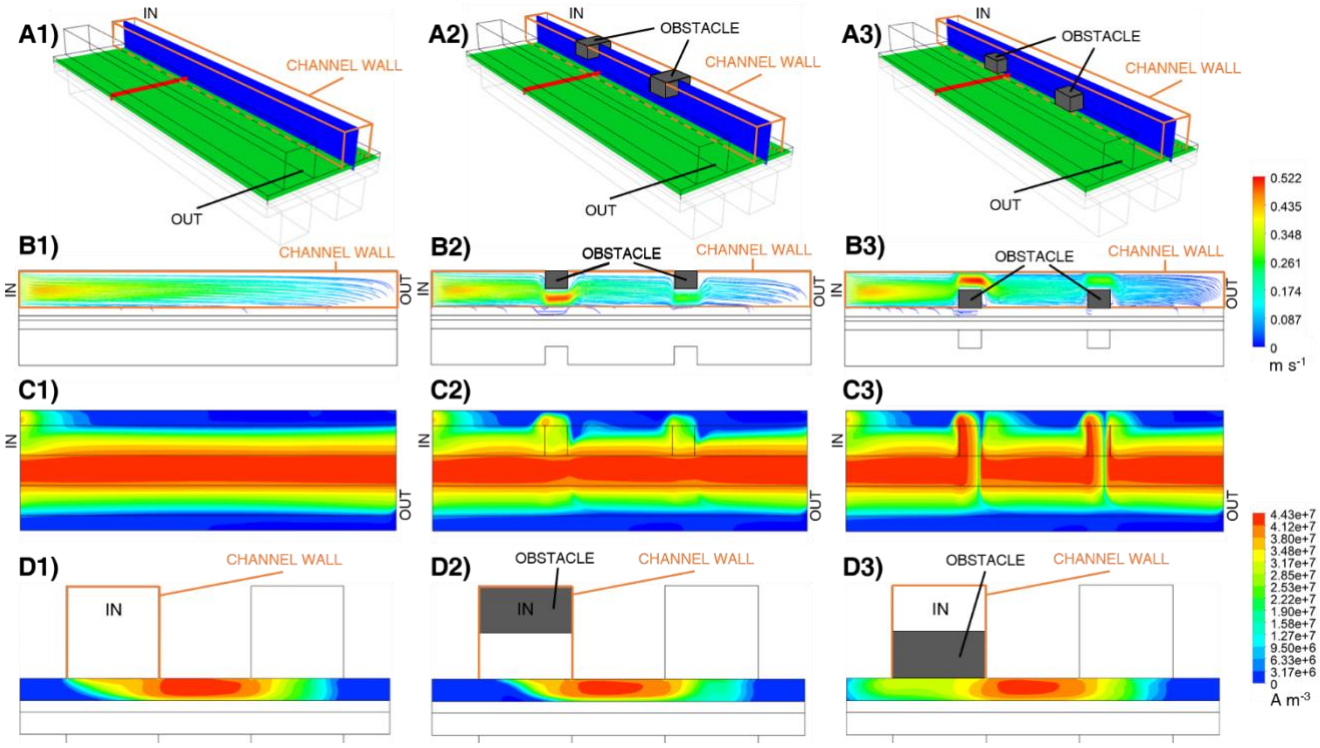

Fig. 4 – A) Simulated geometries with highlighted planes representing the locations of physical quantities illustrated in B), C) and D); B) streamlines of the electrolyte flow on the blue cutting plane; C) contours of volumetric current density on the green cutting plane; D) contours of the volumetric current density on the red cutting plane. Column 1: standard interdigitated; column 2: obstruction #1; column 3: obstruction #2. Length of domain in A), B), C) is scaled for the sake of readability.

Analysing the contours of the volumetric current density at half of the electrode thickness (Fig. 4C2 and Fig. 4C3), it can be noticed that the presence of obstacles in the channel causes an additional area of the electrode, located in correspondence of the obstacle itself, to be characterized by a volumetric current density greater than the one obtained for the standard geometry (Fig. 4C1). In the case of obstruction #2, this beneficial effect is more relevant close to the obstruction due to the increased electric contact with the electrode and moreover it spans also after the obstruction position. Therefore, model simulations evidence that both obstructions improve cell performance, but the #2 is more promising.

Finally, Fig. 4D represents the contour of volumetric current density in the porous electrode on a plane perpendicular to the channel direction, located 1 mm downstream the first obstacle (red plane in Fig. 4A). The electrode portion under the feeding channel interested by higher values of volumetric current density appears enlarged by the presence of the obstruction #2 and spans the entire electrode thickness (Fig. 4D3). Differently the obstruction #1 (Fig. 4D2) reveals a distribution more similar to the standard interdigitated (Fig. 4D1), but with a contraction of the zone of the porous electrode experiencing higher volumetric current density. This implies a reduction of the local performance in the area just after the obstacle #2.

In order to validate model predictions, the following section (Section 4.3) reports the testing results of both obstructions in symmetric cell configuration with positive and negative electrolyte. The effect of obstructions is then evaluated during cycles at different operating current in order to evaluate the evolution of exchanged capacity (Section 4.4).

4.3 Effect of channel obstructions on polarization curves

4.3.1 Symmetric cell with positive electrolyte

The effect of obstructions displacement on polarization curves of symmetric cell with positive electrolyte at 20 ml min^{-1} is reported in Fig. 5. The figure illustrates the effect of obstructions #1 and #2 placed close to electrolyte inlet (X-0-0-0 in Fig. 5A) or outlet (0-0-0-X in Fig. 5B), while all the other investigated combinations are not reported for the sake of brevity and figure readability. In all the investigated configurations, the obstructions are placed in all the feeding channels, creating a pressure difference between each couple of feeding and discharge channels. In Fig. 5 performance with inserts are compared with the performance of the battery without channel obstructions[11] (named 0-0-0-0).

[11] The performance of 0-0-0-0, which reproduces the interdigitated geometry, is lower compared to that reported in Fig. 3A due to the Teflon™ inserts reducing the electric contact between the electrode and the flow-field.

It is worth noting that the two types of obstruction induce different effect according to their relative position with respect to electrolyte inlet: in particular, obstruction #1 presents better performance when is close to electrolyte outlet (Fig. 5B), while obstruction #2 is more effective near electrolyte inlet (Fig. 5A).

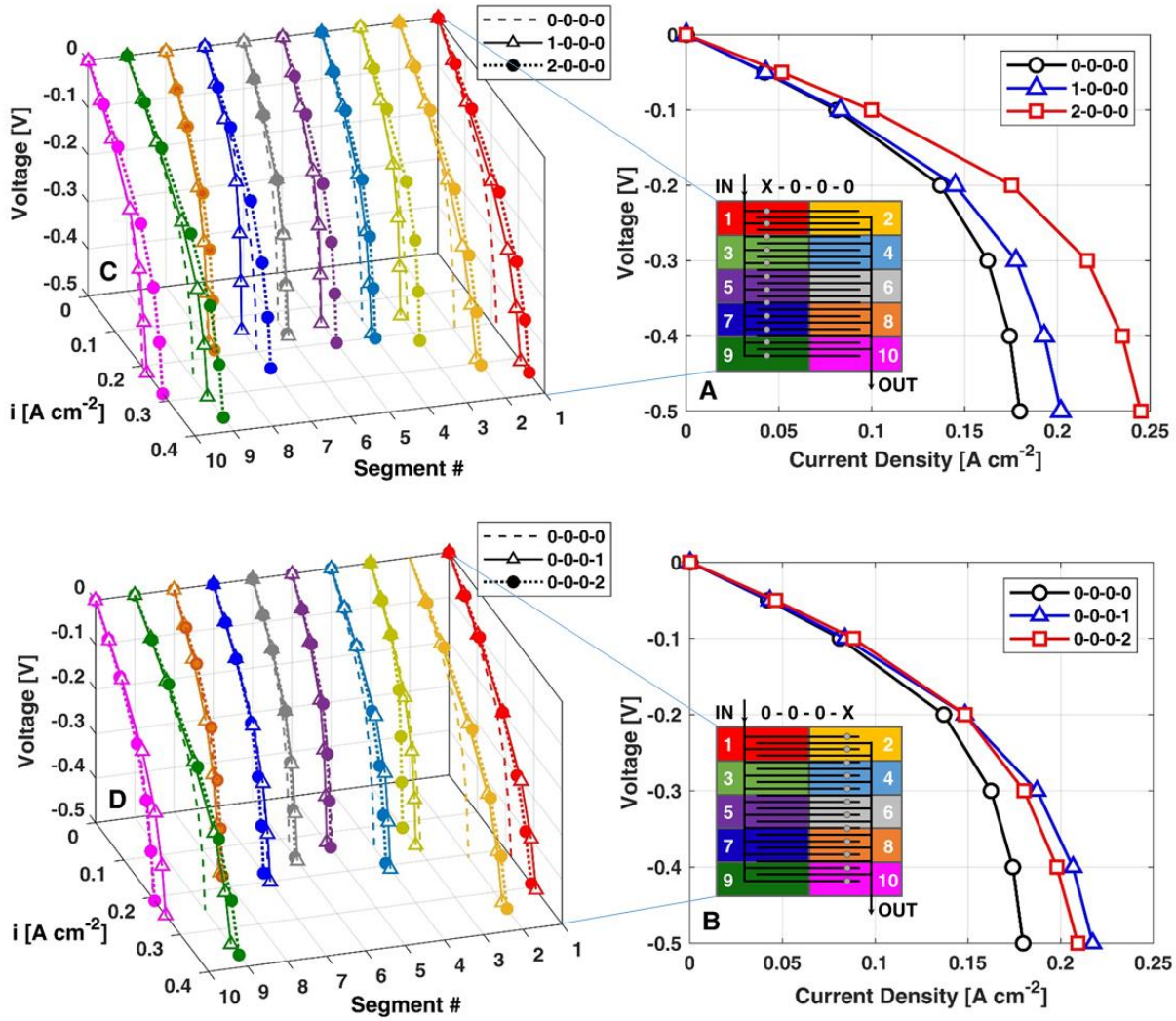

Fig. 5 – Polarization curves at 20 ml min^{-1} with channel obstructions in Teflon™ placed in different locations: A) obstructions close to electrolyte inlet; B) obstructions close to electrolyte outlet; C) local performance with obstructions close to electrolyte inlet; D) local performance with obstructions close to electrolyte outlet. Reactants stoichiometry at 20 ml min^{-1} and 0.2 A cm^{-2} is around 5.

This finding is consistent with model results discussed in Section 4.2, which highlight for the obstruction #2 a larger share of electrolyte flowing downstream the obstruction with higher velocity and a portion of the electrode located after the obstruction characterized by higher

volumetric current density. Therefore, the location of obstruction #2 that maximizes the electrode portion interested by these induced beneficial effects is near the channel inlet. On the contrary, when obstruction #1 is near the outlet, the area of electrode interested by an enhanced pressure drop and the one interested by lower velocity are maximized and minimized, respectively. However, in this position (Fig. 5B), the performance difference with obstruction #2 is limited. Considering the absolute cell performance, regardless of obstruction position and typology, the presence of a channel obstruction improves the battery performance, supporting again model predictions.

In order to confirm the proposed interpretation and to provide an insight into the origin of such a different behaviour, the corresponding local polarization curves are depicted in Fig. 5C-D, which compares throughout battery active area the effect of the two different obstructions placed at the same location. It is worth emphasizing that the local performance is regulated by a complex interplay between kinetic and mass transport mechanisms occurring at various scales (channel, electrode, pore, active site) with different intensity. Moreover, all the regions of battery active area interact with each other: in example the increased performance of a region of the cell could limit the performance in another region, resulting in a complex interpretation of local experimental data. For this reason, in Fig. 5C-D all local polarization curves do not exactly show the same behaviour, but a general trend can be observed.

In Fig. 5C the obstructions are placed close to electrolyte inlet: it is evident that obstruction #2 presents better performance throughout cell active area. In particular, the performance difference with obstruction #1 is higher in the odd numbered segments. Coherently with the modelling analyses reported in Section 4.2, obstruction #1 is less effective in the cell region just after its location: in correspondence of the obstruction #1 a relevant fraction of not reacted electrolyte is forced to permeate through the porous electrode and the remaining reactant is made available in the region of active area downstream the obstruction with a reduced velocity.

This hinders the performance of the downstream segments and penalizes the central region, already characterized by lower velocity, as obtained with the model and discussed in Section 4.1. On the contrary, obstruction #2 allows a relevant fraction of the electrolyte to continue its flow along the feeding channel and at the same time induces a localized pressure drop between feeding and discharge channels, enhancing the electrolyte permeation through the porous electrode (i.e. *under-the-rib* fluxes). In general, considering local performance with interdigitated geometry (0-0-0-0 in Fig. 5C), the presence of obstructions close to electrolyte inlet increases battery performance all over the active area.

Fig. 5D reports the local performance with obstructions placed near electrolyte outlet. In this case there is not a clear trend in the behaviour of the segments and in fact, as reported in Fig. 5B, the global performance of 0-0-0-1 is comparable with the one of 0-0-0-2. With obstruction #1 close to the outlet, the region of cell active area downstream the obstruction, which is characterized by lower velocity and performance, is limited. Instead, the obstruction #2 is less effective compared to its positioning near electrolyte inlet since the fraction of not reacted electrolyte that can continue its flow along the channel presents a lower concentration of charged ions (considering discharge). This limits the positive effect of this type of obstruction on cell performance. Moreover, the performance difference compared to interdigitated geometry (0-0-0-0 in Fig. 5D) is evident in a limited region of cell active area, in particular close to electrolyte inlet and outlet, that are characterized by a higher electrolyte velocity [29].

The positions of channel obstructions reported in Fig. 5 have been selected in order to provide an experimental verification of model simulations for the design of innovative flow fields, reported in Section 4.2. The choice of Teflon™ as manufacturing material was driven by the necessity to guarantee electric insulation among all the segments of the cell (Fig. 1) and thus provide a reliable local resolution of current density distribution, as explained in the experimental section. For the sake of brevity this work does not report all the investigated

obstacles configurations, varying their number and position in the flow-field (Fig. 1). Fig. B1 illustrates polarization curves of the best configuration adopting obstacle #1 and #2 at different electrolyte flow rates. The introduction of obstacles in all the available locations over the flow field turned out to be best solution and configuration 2-2-2-2 showed higher performance with a minor pressure drop increase.

In the following part of this work, since the local performance are not analysed any more, all the presented data are obtained with obstructions made in graphite in order to avoid the loss of electric contact between electrodes and flow plates. All the tests made with Teflon™ inserts have been repeated with inserts made in graphite, confirming the observed trends on global performance. Fig. 6 reports the comparison of 2-2-2-2 with conventional geometries at different electrolyte flow rates, both in term of performance (Fig. 6A-B) and pressure drops (Fig. 6C).

Considering the comparison with the interdigitated geometry (Fig. 6A), it is evident that at the same flow rate 2-2-2-2 shows better performance, maintaining meanwhile an acceptable pressure drop increase (Fig. 6C). In particular, the 2-2-2-2 at 40 ml min^{-1} has similar performance with the interdigitated at 90 ml min^{-1}: in these two conditions the pressure drops are nearly equal, but auxiliary consumption is roughly the double for the interdigitated geometry.

The comparison of 2-2-2-2 with serpentine geometry is not performed at the same flow rate (Fig. 6B), since pressure drops between the two flow fields are considerably different (Fig. 6C). Moreover, due to limitations of the pump, it is not possible to operate the symmetric cell with serpentine flow field at a flow rate higher than 30 ml min^{-1}. 2-2-2-2 at 40 ml min^{-1} presents performance similar to serpentine at 30 ml min^{-1}, but the pressure drops are reduced by 80%. At 90 ml min^{-1} 2-2-2-2 outperforms serpentine geometry and exhibits 60% lower pressure drops.

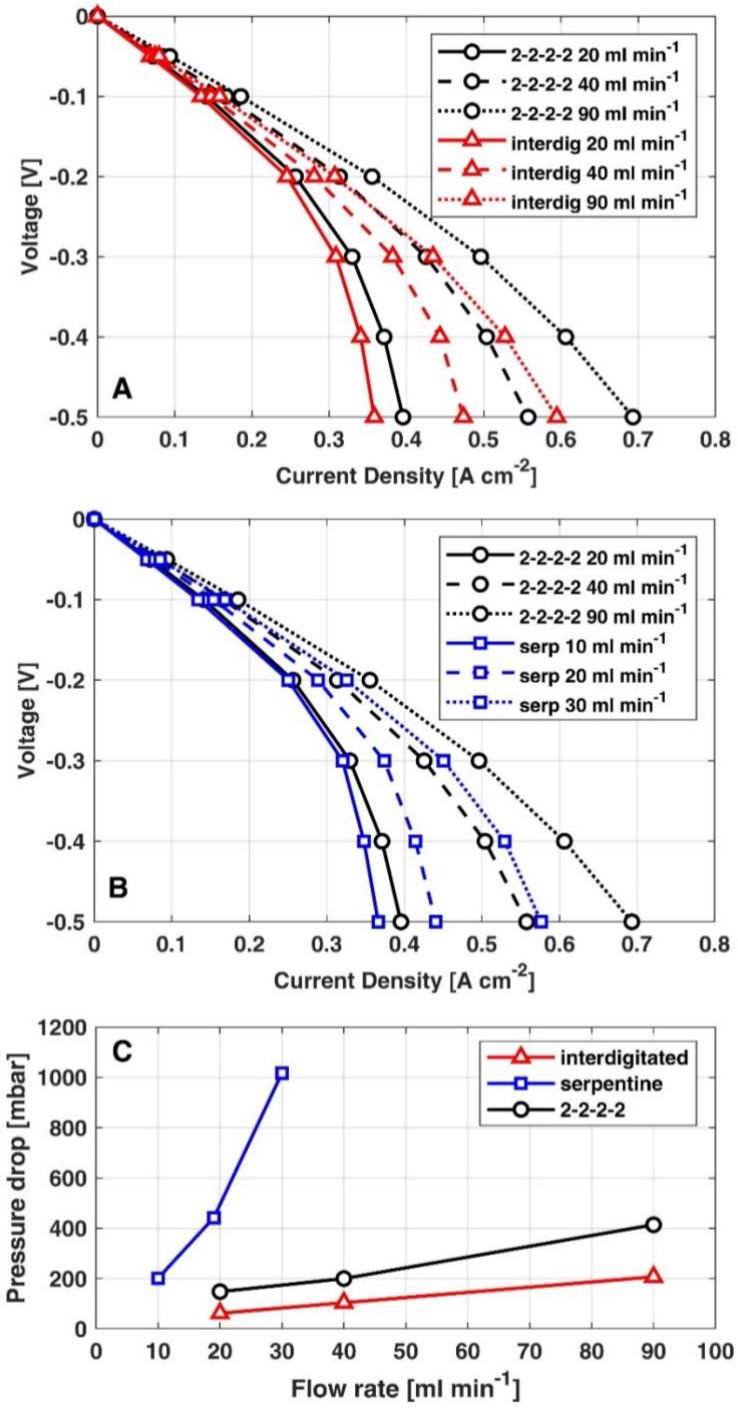

Fig. 6 – Symmetric cell with positive electrolyte: A) polarization curves adopting interdigitated and 2-2-2-2 made in graphite; B) polarization curves adopting serpentine and 2-2-2-2 made in graphite; C) pressure drops of interdigitated, serpentine and 2-2-2-2 made in graphite. Reactants stoichiometry at 20 ml min^{-1} and 0.4 A cm^{-2} is around 2.5.

The developed innovative geometry 2-2-2-2 is demonstrated to be a good compromise between performance and pressure drops considering symmetric cell performance with positive electrolyte. In the following, the innovative flow field is tested in symmetric cell with negative electrolyte.

4.3.2 Symmetric cell with negative electrolyte

Fig. 7A reports the polarization curves of symmetric cell with negative electrolytes at 20 ml min^{-1} for the different flow fields. Pressure drops are not reported for the sake of brevity since similar to the ones of the positive electrolyte (Fig. 6C). Even if the current density range is more limited compared to symmetric cell with positive electrolyte (Fig. 6A-B), 2-2-2-2 outperforms interdigitated geometry and presents similar performance compared to the serpentine flow field, that just presents a slightly higher maximum current density despite the considerably greater pressure drops. Since the operation of negative electrode is hindered by kinetic losses [45] and the resulting range of operating current density is limited, at higher flow rate (Fig. 7B) the differences among the flow fields tends to decrease, with the 2-2-2-2 showing slightly lower performance compared to serpentine geometry. Thus, the developed geometry turned out to be effective also in symmetric cell with negative electrolyte.

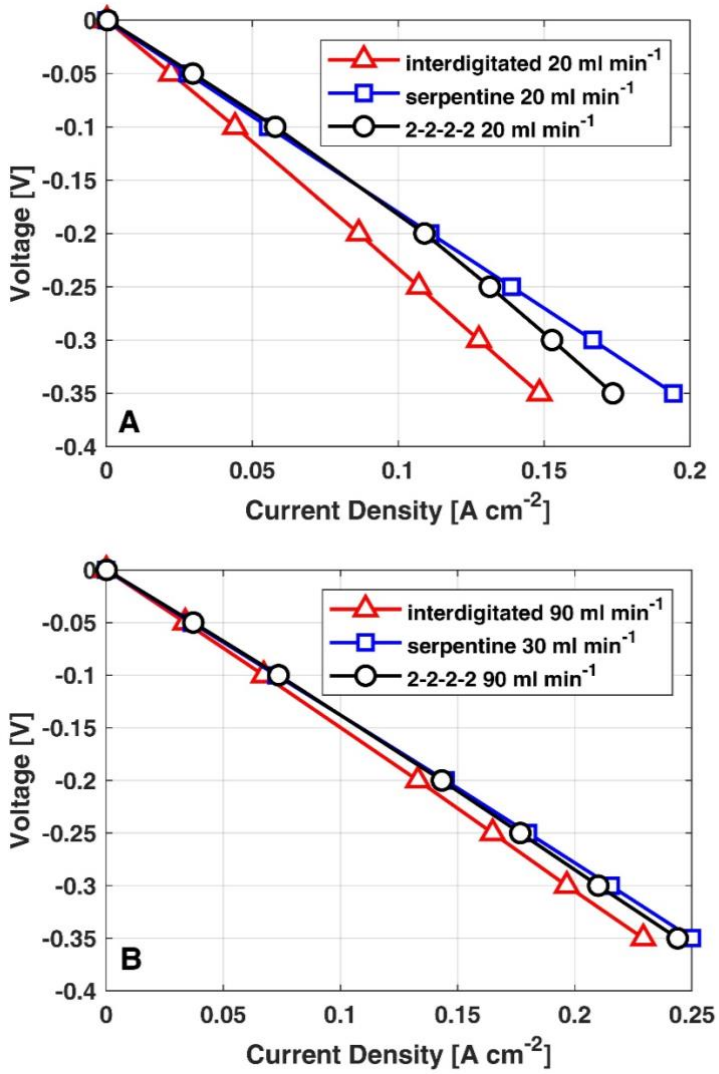

Fig. 7 – Symmetric cell with negative electrolyte adopting interdigitated, serpentine and 2-2-2-2 made in graphite: A) polarization curves at 20 ml min^{-1}; B) polarization curves at the maximum flow rate; Reactants stoichiometry at 20 ml min^{-1} and 0.2 A cm^{-2} is around 5.

The experimental hardware described and developed in this work (Section 2.1), that permits to easily change the number and position of channel obstructions throughout cell active area, turned out to be a flexible tool to study the effect of flow field modifications on battery performance, also providing an insight on local current density distribution. Considering performance in symmetric cell with both positive and negative electrolytes, 2-2-2-2 is the best flow field among all the investigated configurations with channel obstructions. In the following section the effect of 2-2-2-2 geometry is evaluated during cycles at different operating current.

4.4 Effect of channel obstructions on charge-discharge cycles

Symmetric cell configuration is an experimental technique that permits to perform a high number of experimental tests without critical issues in the management of electrolyte SoC, that in the tank is around 50%. However, during charge-discharge cycles electrolyte SoC in the tanks is not constant and usually varies between 10% and 90% [46], depending on the considered operating condition and the adopted cut-off voltages. Moreover, VRFB real operation is affected by cross-contamination [47] and the flow field, along with the operating current [39,48,49], is crucial in the definition of electrolyte velocity and concentration profiles at the electrode-membrane interface. The effect of electrolytes imbalance induced by vanadium cross-over on battery performance and exchanged capacity thus results from a mutual interaction between different physical processes. For these reasons, the configuration 2-2-2-2 has been tested during cycles at both 0.1 and 0.2 A cm^{-2} and subsequently compared with interdigitated and serpentine geometries.

The evolution of the exchanged capacity at 0.1 A cm^{-2} and 0.2 A cm^{-2} is reported in Fig. 8 A and Fig. 8B, respectively. The values at 1st cycle are less affected by electrolyte imbalance and are coherent with the performance analysis at constant flow rate of symmetric cell with negative electrolyte (Fig. 7A), that mainly regulates the operation of the system [45]. At 0.1 A cm^{-2} (Fig. 8A) there is no significant difference in the exchanged capacity during 1st cycle, with interdigitated showing slightly lower values, while at 0.2 A cm^{-2} serpentine outperforms the other configurations and interdigitated exhibits poor performance. However, serpentine exhibits a more intense decreasing trend during cycles (Fig. 8A-B), most probably related to the higher electrolyte velocities compared to the other flow field configurations. In fact, interdigitated and 2-2-2-2 present comparable velocities in the distribution channels and, excluding the first 10 cycles of interdigitated at 0.1 A cm^{-2} (Fig. 8A), the resulting trend of exchanged capacity is similar.

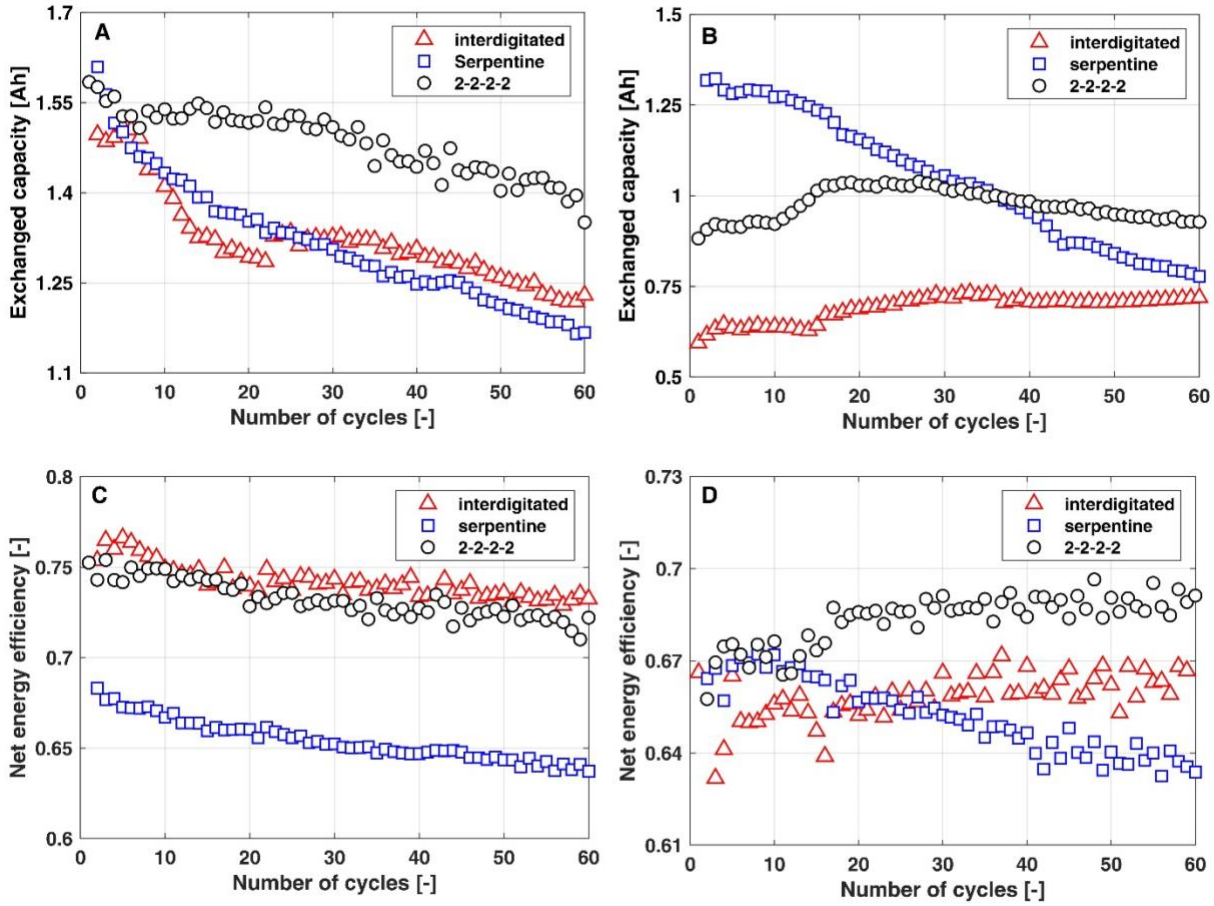

Fig. 8 – Evolution during cycles at 40 ml min^{-1} with interdigitated, serpentine and 2-2-2-2 made in graphite: A) exchanged capacity at 0.1 A cm^{-2}; B) exchanged capacity at 0.2 A cm^{-2}; C) net energy efficiency at 0.1 A cm^{-2}; D) net energy efficiency at 0.2 A cm^{-2}.

Fig. 8C-D reports the corresponding net energy efficiency, that takes into account auxiliaries consumption. Assuming pump efficiency equal to 0.9 and considering the measured pressure drops, the resulting values of auxiliaries' consumption are 288 mW for serpentine, 30 mW for 2-2-2-2 and 15 mW for interdigitated. At 0.1 A cm^{-2}, the resulting energy efficiency loss is 9.2% for serpentine, 1.7% for 2-2-2-2 and 1.1% for interdigitated. Thus, at 0.1 A cm^{-2} (Fig. 8C), serpentine distributor presents considerably lower net energy efficiency due to the increased auxiliaries' consumption. Conversely, interdigitated is less affected by pumping losses and the net energy efficiency is 1-2% higher compared to 2-2-2-2 geometry, that anyway permits to exchange a higher amount of capacity (Fig. 8A). At 0.2 A cm^{-2} (i.e., higher specific power), the weight of auxiliary consumption is less relevant and the resulting energy efficiency loss is 4.4%

for serpentine, 0.8% for 2-2-2-2 and 0.5% for interdigitated. In Fig. 8D, at the beginning of the cycles serpentine geometry presents similar values of net energy efficiency compared to the other configurations, while towards the end of the cycles the values are lower due to the increased capacity decay induced by vanadium cross-over (Fig. 8B). At 0.2 A cm^{-2}, the higher auxiliaries consumption of 2-2-2-2 compared to interdigitated is balanced by a relatively greater performance increase and consequently 2-2-2-2 presents the higher net energy efficiency, confirming that the proposed geometry has a good trade-off between performance, pressure drops and evolution of exchanged capacity in a different range of operating conditions. The effectiveness of the developed innovative geometry based on the local introduction of obstructions in the feeding channels can be further exploited in cell with a size representative of real systems, in which the impact of local reactants starvation and pressure drop are more relevant. This will be investigated by the authors in a future work.

5. Conclusions

This work presented the design of improved flow fields with the aid of a complete 3D VRFB model. The model couples a traditional fluid dynamic analysis of the electrolyte with the electrochemistry of the reactions involved and simulates the influence of both single serpentine and interdigitated flow field in a cell with 25 cm^2 active area. The model has been extensively validated with respect to local polarization curves collected on a segmented cell hardware and is thus used to design two different channel obstructions: the first one (obstruction #1) is located at the channel wall, while the second one (obstruction #2) is placed close to electrode interface. Both obstructions create a localized pressure difference between channels, enhancing electrolyte permeation through porous electrode. Finally, improved flow fields are tested, highlighting obstructions effect on both global and local cell performance. The main conclusions of the work are the following:

- In correspondence of obstruction #1 a relevant share of not reacted electrolyte is forced to permeate through the porous electrode and the remaining is made available in the region downstream its location with a reduced velocity. Experimental polarization curves confirm that obstruction #1 is more effective when is placed close to electrolyte outlet.
- In correspondence of obstruction #2 a relevant part of the not reacted electrolyte continues its flow along the feeding channel and at the same time a localized pressure drop between feeding and discharge channels is induced. Experimental polarization curves demonstrate that obstruction #2 is more effective when is placed close to electrolyte inlet and it presents higher global performance compared to obstruction #1.
- The configuration 2-2-2-2 is the one providing the best trade-off between performance and pressure drops. In symmetric cell with positive electrolyte 2-2-2-2 outperforms serpentine geometry and exhibits 60% lower pressure drops, while, with respect to interdigitated, 2-2-2-2 exhibits similar performance in front of a 50% reduction of auxiliaries' consumption.
- Considering symmetric cell with negative electrolyte, the effect of channel obstructions is less evident due to the sluggish electrode kinetic and the limited range of operating current. Anyway configuration 2-2-2-2 shows similar performance compared to serpentine geometry, but it permits to considerably reduce pressure drop.
- During cycles at 40 ml min^{-1}, serpentine suffers from high auxiliaries' consumption and exhibits a faster decay of the exchanged capacity, most probably induced by the higher electrolyte velocities in the porous electrodes. Interdigitated geometry is less affected by auxiliaries' consumption, but the performance at 0.2 A cm^{-2} is considerably lower compared to the other flow fields. Instead, the developed 2-2-2-2 geometry guarantees

a good trade-off among efficiency, auxiliary consumption and exchanged capacity in a different range of operating conditions.

Appendix A

Fig. A1A and A1B illustrates the model domain with serpentine and interdigitated flow field, respectively. The different domains in the plane X-Z and the corresponding nomenclature are highlighted in Fig. A1C.

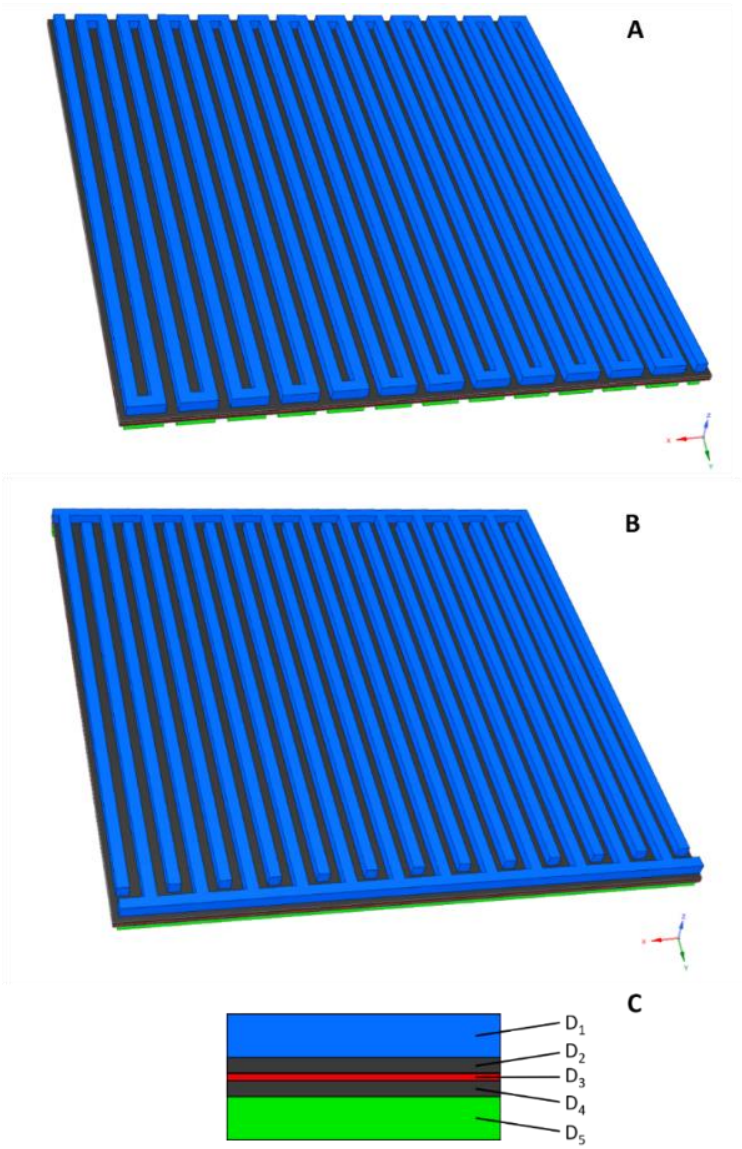

Fig. A1 – Model domain: A) serpentine; B) interdigitated; C) domain nomenclature.

Appendix B

Fig. B1 compares performance of 0-0-0-0, 1-1-1-1 and 2-2-2-2 configurations with obstacles made in Teflon™ in symmetric cell with positive electrolyte. At 20 ml min^{-1} the presence of obstacles in all the four available positions in the flow field (Fig. B1A) considerably enhances battery performance: the performance increase is higher compared to the one obtained with obstacles placed just at electrolyte inlet or outlet (Fig. 5A-B). The configuration 2-2-2-2 exhibits higher performance at all the investigated flow rates (Fig. B1B-C) and furthermore the corresponding pressure drops are minor compared to the configuration with obstacles #1 (Fig. B1D). The pressure drop increase induced by the presence of obstacles in the feeding channels is acceptable for system operation: the impact of auxiliaries consumption is described in Section 4.4.

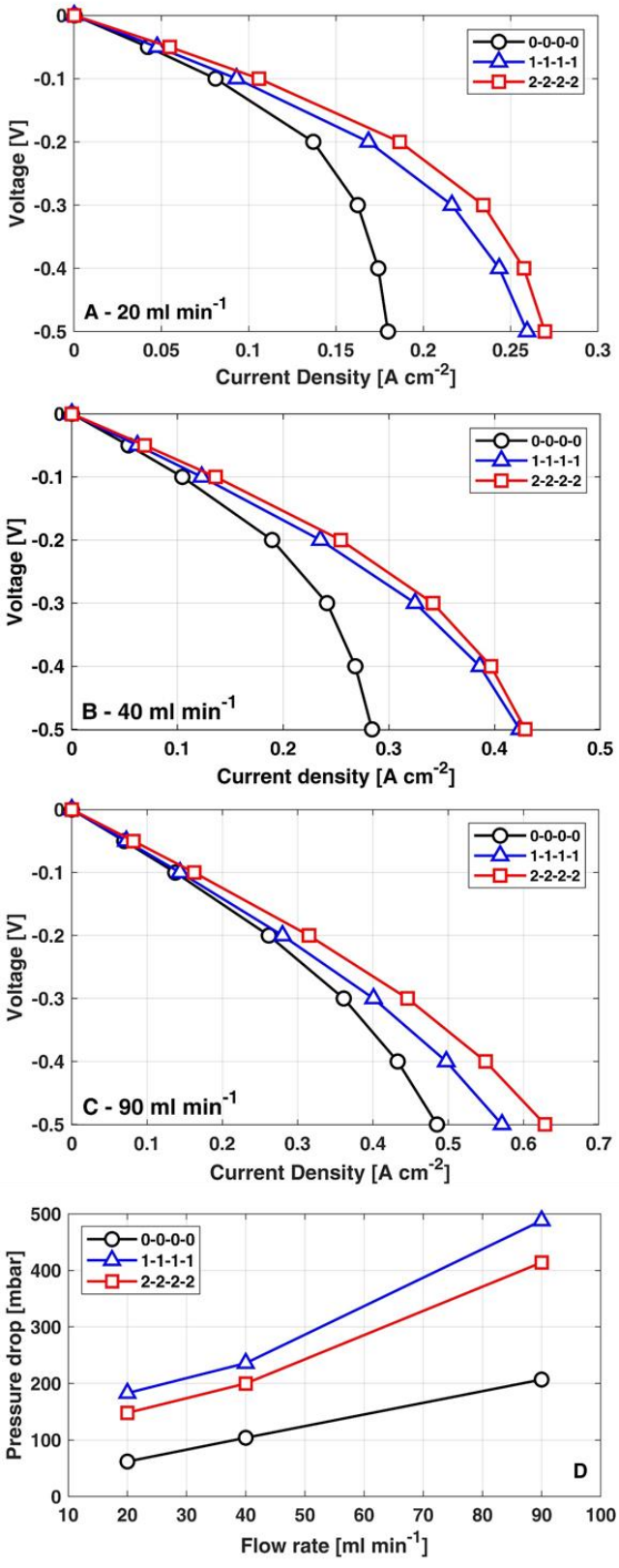

Fig. B1 – Comparison between 0-0-0-0, 1-1-1-1 and 2-2-2-2 with channel obstructions in Teflon™ in symmetric cell with positive electrolyte: A) polarization curves at 20 ml min^{-1}; B) polarization curves at 40 ml min^{-1}; C) polarization curves at 90 ml min^{-1}; D) pressure drops.

Acknowledgement

This work was partially funded by ENI S.p.A. in the framework of the research project entitled: "Batterie a flusso al vanadio innovative" (OdL 4310296114 of 06/09/2018). The authors acknowledge Andrea Lazzaroni and Alessandro Zinni for support with experimental measurements and model validation.

References

[1] Alotto P, Guarnieri M, Moro F. Redox flow batteries for the storage of renewable energy: A review. Renew Sustain Energy Rev 2014;29:325–35. doi:10.1016/j.rser.2013.08.001.

[2] Soloveichik GL. Flow Batteries: Current Status and Trends. Chem Rev 2015;115:11533–58. doi:10.1021/cr500720t.

[3] Parasuraman A, Lim TM, Menictas C, Skyllas-Kazacos M. Review of material research and development for vanadium redox flow battery applications. Electrochim Acta 2013;101:27–40. doi:10.1016/j.electacta.2012.09.067.

[4] Weber AZ, Mench MM, Meyers JP, Ross PN, Gostick JT, Liu Q. Redox flow batteries: A review. J Appl Electrochem 2011;41:1137–64. doi:10.1007/s10800-011-0348-2.

[5] Wu M, Liu M, Long G, Wan K, Liang Z, Zhao TS. A novel high-energy-density positive electrolyte with multiple redox couples for redox flow batteries. Appl Energy 2014;136:576–81. doi:10.1016/j.apenergy.2014.09.076.

[6] Chakrabarti MH, Brandon NP, Hajimolana SA, Tariq F, Yufit V, Hashim MA, et al. Application of carbon materials in redox flow batteries. J Power Sources 2014;253:150–66. doi:10.1016/j.jpowsour.2013.12.038.

[7] Zakeri B, Syri S. Electrical energy storage systems: A comparative life cycle cost analysis. Renew Sustain Energy Rev 2015;42:569–96. doi:https://doi.org/10.1016/j.rser.2014.10.011.

[8] Zeng YK, Zhao TS, An L, Zhou XL, Wei L. A comparative study of all-vanadium and iron-chromium redox flow batteries for large-scale energy storage. J Power Sources 2015;300:438–43. doi:10.1016/j.jpowsour.2015.09.100.

[9] Arenas LF, Ponce de León C, Walsh FC. Pressure drop through platinized titanium porous electrodes for cerium-based redox flow batteries. AIChE J 2018;64:1135–46. doi:10.1002/aic.16000.

[10] Kim S, Thomsen E, Xia G, Nie Z, Bao J, Recknagle K, et al. 1 kW/1 kWh advanced vanadium redox flow battery utilizing mixed acid electrolytes. J Power Sources 2013;237:300–9. doi:10.1016/j.jpowsour.2013.02.045.

[11] Minke C, Dorantes Ledesma MA. Impact of cell design and maintenance strategy on life cycle costs of vanadium redox flow batteries. J Energy Storage 2019;21:571–80. doi:10.1016/j.est.2018.12.019.

[12] Arenas LF, Ponce de León C, Walsh FC. Engineering aspects of the design, construction and performance of modular redox flow batteries for energy storage. J Energy Storage 2017;11:119–53. doi:10.1016/j.est.2017.02.007.

[13] Houser J, Pezeshki A, Clement JT, Aaron D, Mench MM. Architecture for improved mass transport and system performance in redox flow batteries. J Power Sources 2017;351:96–105. doi:10.1016/j.jpowsour.2017.03.083.

[14] Lisboa KM, Marschewski J, Ebejer N, Ruch P, Cotta RM, Michel B, et al. Mass transport enhancement in redox flow batteries with corrugated fluidic networks. J Power Sources 2017;359:322–31. doi:10.1016/j.jpowsour.2017.05.038.

[15] Zeng Y, Li F, Lu F, Zhou X, Yuan Y, Cao X, et al. A hierarchical interdigitated flow field design for scale-up of high-performance redox flow batteries. Appl Energy 2019;238:435–41. doi:10.1016/j.apenergy.2019.01.107.

[16] Akuzum B, Alparslan YC, Robinson NC, Agar E, Kumbur EC. Obstructed flow field

designs for improved performance in vanadium redox flow batteries. J Appl Electrochem 2019;49:551–61. doi:10.1007/s10800-019-01306-1.

[17] Brown CJ, Pletcher D, Walsh FC, Hammond JK, Robinson D. Local mass transport effects in the FM01 laboratory electrolyser. J Appl Electrochem 1992;22:613–9. doi:10.1007/BF01092609.

[18] Brown CJ, Pletcher D, Walsh FC, Hammond JK, Robinson D. Studies of space-averaged mass transport in the FM01-LC laboratory electrolyser. J Appl Electrochem 1993;23:38–43. doi:10.1007/BF00241573.

[19] Castañeda LF, Walsh FC, Nava JL, Ponce de León C. Graphite felt as a versatile electrode material: Properties, reaction environment, performance and applications. Electrochim Acta 2017;258:1115–39. doi:10.1016/j.electacta.2017.11.165.

[20] Zheng Q, Li X, Cheng Y, Ning G, Xing F, Zhang H. Development and perspective in vanadium flow battery modeling. Appl Energy 2014;132:254–66. doi:10.1016/j.apenergy.2014.06.077.

[21] Oh K, Yoo H, Ko J, Won S, Ju H. Three-dimensional, transient, nonisothermal model of all-vanadium redox flow batteries. Energy 2015;81:3–14. doi:10.1016/j.energy.2014.05.020.

[22] Ma X, Zhang H, Xing F. A three-dimensional model for negative half cell of the vanadium redox flow battery. Electrochim Acta 2011;58:238–46. doi:10.1016/j.electacta.2011.09.042.

[23] Wang Y, Cho SC. Analysis and Three-Dimensional Modeling of Vanadium Flow Batteries. J Electrochem Soc 2014;161:A1200–12. doi:10.1149/2.0061409jes.

[24] Chen JQ, Wang BG, Lv HL. Numerical Simulation and Experiment on the Electrolyte Flow Distribution for All Vanadium Redox Flow Battery. Adv Mater Res 2011;236–238:604–7. doi:10.4028/www.scientific.net/AMR.236-238.604.

[25] Ozgoli HA, Elyasi S, Mollazadeh M. Hydrodynamic and electrochemical modeling of vanadium redox flow battery. Mech Ind 2015;16:201. doi:10.1051/meca/2014071.

[26] Zheng Q, Zhang H, Xing F, Ma X, Li X, Ning G. A three-dimensional model for thermal analysis in a vanadium flow battery. Appl Energy 2014;113:1675–85. doi:10.1016/j.apenergy.2013.09.021.

[27] Yin C, Gao Y, Guo S, Tang H. A coupled three dimensional model of vanadium redox flow battery for flow field designs. Energy 2014;74:886–95. doi:10.1016/j.energy.2014.07.066.

[28] Xu Q, Zhao TS, Leung PK. Numerical investigations of flow field designs for vanadium redox flow batteries. Appl Energy 2013;105:47–56. doi:10.1016/j.apenergy.2012.12.041.

[29] Messaggi M, Canzi P, Mereu R, Baricci A, Inzoli F, Casalegno A, et al. Analysis of flow field design on vanadium redox flow battery performance: Development of 3D computational fluid dynamic model and experimental validation. Appl Energy 2018;228:1057–70. doi:10.1016/j.apenergy.2018.06.148.

[30] Hsieh WY, Leu CH, Wu CH, Chen YS. Measurement of local current density of all-vanadium redox flow batteries. J Power Sources 2014;271:245–51. doi:10.1016/j.jpowsour.2014.06.081.

[31] Clement JT, Zawodzinski TA, Mench MM. Measurement of Localized Current Distribution in a Vanadium Redox Flow Battery. ECS Trans 2014;58:9–16. doi:10.1149/05837.0009ecst.

[32] Clement JT, Aaron DS, Mench MM. In Situ Localized Current Distribution Measurements in All-Vanadium Redox Flow Batteries. J Electrochem Soc 2016;163:A5220–8. doi:10.1149/2.0241601jes.

[33] Bhattarai A, Wai N, Schweiss R, Whitehead A, Scherer GG, Ghimire PC, et al. Study of

flow behavior in all-vanadium redox fl ow battery using spatially resolved voltage distribution. J Power Sources 2017;360:443–52. doi:10.1016/j.jpowsour.2017.06.039.

[34] Ghimire PC, Bhattarai A, Schweiss R, Scherer GG, Wai N, Yan Q. A comprehensive study of electrode compression effects in all vanadium redox flow batteries including locally resolved measurements. Appl Energy 2018;230:974–82. doi:10.1016/j.apenergy.2018.09.049.

[35] Messaggi M, Rabissi C, Gambaro C, Meda L, Casalegno A, Zago M. Investigation of vanadium redox flow batteries performance through locally-resolved polarisation curves and impedance spectroscopy: Insight into the effects of electrolyte, flow field geometry and electrode thickness. J Power Sources 2020;449:227588. doi:10.1016/j.jpowsour.2019.227588.

[36] Schweiss R, Meiser C, Damjanovic T, Galbiati I, Haak N. SIGRACET® Gas Diffusion Layers for PEM Fuel Cells, Electrolyzers and Batteries (White Paper) 2016.

[37] Aaron DS, Liu Q, Tang Z, Grim GM, Papandrew AB, Turhan A, et al. Dramatic performance gains in vanadium redox flow batteries through modified cell architecture. J Power Sources 2012;206:450–3. doi:10.1016/j.jpowsour.2011.12.026.

[38] Pezeshki AM, Sacci RL, Delnick FM, Aaron DS, Mench MM. Elucidating effects of cell architecture, electrode material, and solution composition on overpotentials in redox flow batteries. Electrochim Acta 2017;229:261–70. doi:10.1016/j.electacta.2017.01.056.

[39] Cecchetti M, Casalegno A, Zago M. Local potential measurement through reference electrodes in vanadium redox flow batteries: Evaluation of overpotentials and electrolytes imbalance. J Power Sources 2018;400:218–24. doi:10.1016/j.jpowsour.2018.08.033.

[40] Knehr KW, Agar E, Dennison CR, Kalidindi AR, Kumbur EC. A Transient Vanadium Flow

Battery Model Incorporating Vanadium Crossover and Water Transport through the Membrane. J Electrochem Soc 2012;159:A1446–59. doi:10.1149/2.017209jes.

[41] Schmal D, Van Erkel J, Van Duin PJ. Mass transfer at carbon fibre electrodes. J Appl Electrochem 1986;16:422–30. doi:10.1007/BF01008853.

[42] Yamamura T, Watanabe N, Yano T, Shiokawa Y. Electron-Transfer Kinetics of Np^{3+}/ Np^{4+}, NpO_2^+/NpO_2^{2+}, V^{2+}/V^{3+}, and VO^{2+}/VO_2^+ at Carbon Electrodes. J Electrochem Soc 2005;152:A830. doi:10.1149/1.1870794.

[43] Xu Q, Zhao TS, Zhang C. Effects of SOC-dependent electrolyte viscosity on performance of vanadium redox flow batteries. Appl Energy 2014;130:139–47. doi:10.1016/j.apenergy.2014.05.034.

[44] Houser J, Clement J, Pezeshki A, Mench MM. Influence of architecture and material properties on vanadium redox flow battery performance. J Power Sources 2016;302:369–77. doi:10.1016/j.jpowsour.2015.09.095.

[45] Cecchetti M, Messaggi M, Donazzi A, Facibeni A, Russo V, Casari CS, et al. A combined morphological and electrochemical characterization of carbon electrodes in vanadium redox flow batteries: Insights into positive and negative electrode performance. Electrochim Acta 2020;329:135143. doi:10.1016/j.electacta.2019.135143.

[46] Akter M, Li Y, Bao J, Skyllas-Kazacos M, Rahman M. Optimal Charging of Vanadium Redox Flow Battery with Time-Varying Input Power. Batteries 2019;5:20. doi:10.3390/batteries5010020.

[47] Cecchetti M, Ebaugh TA, Yu H, Bonville L, Gambaro C, Meda L, et al. Design and Development of an Innovative Barrier Layer to Mitigate Crossover in Vanadium Redox Flow Batteries. J Electrochem Soc 2020;167:130535. doi:10.1149/1945-7111/abbbbb.

[48] Pugach M, Vyshinsky V, Bischi A. Energy efficiency analysis for a kilo-watt class vanadium redox flow battery system. Appl Energy 2019;253:113533.

doi:10.1016/j.apenergy.2019.113533.

[49] Trovò A, Picano F, Guarnieri M. Comparison of energy losses in a 9 kW vanadium redox flow battery. J Power Sources 2019;440:227144. doi:10.1016/j.jpowsour.2019.227144.